A simulation-based study of BBB-on-a-chip Permeability Tuning by Induced Electric Field

SAMET AYTEKIN

Supervisors

Prof. Josep Samitier Marti

Dr. Monica Mir

Co-supervisor

Prof. Jeroen Lammertyn

To my father…

Now it's time to finally rest, dad.

ACKNOWLEDGEMENTS

First and foremost, I would like to present my most thankful wishes to my daily supervisor, Dr. Monica Mir. This thesis would not have been possible without her deep knowledge over the subject, on-point advices and in-time actions that saved the day quite often. With her patience, understanding and daily-based support, she showed me what it really means to be the supervisor that everybody needs. She always looked after me and the other students who took part in this project, and she took the right decisions even when the world had gone crazy. Hence the second thanks go to that little virus, COVID-19; without it, this project would have looked entirely different, and major implications revealed in this thesis would have never come to life.

Next, I would like to thank Prof. Josep Samitier, who was always, among his extremely busy schedule, willing to listen my never-ending presentations and gave me the most invaluable comments. I could only dream of being such a strong figure he really is and of having achievements he had in his life. It was a great honor to be a part of his family.

I would like to thank Prof. Romen Rodriguez, who voluntarily spent so much time to teach me how to use COMSOL from scratch; without him, I could not have been able to construct even a straight line. I would also like to thank my co-supervisor, Prof. Jeroen Lammertyn, not only for accepting to supervise my final thesis, but also for everything he taught me in KU Leuven, which, by all means, changed my entire future career.

Even though we spent such a short time together, I would like to thank my labmates, who not only taught me the initial experiments, which were doomed to be halted, but also showed me how a lab makes a real home where you feel happy, safe and always supported. I would like to thank Sujey Palma for calming me down every time I got dramatic; Inês Pereira for helping me cut down my bread consumption; Miriam Funes for literally being the nicest person on Earth; and Clara Alcon, for every lab needs its queen and she holds the crown. This list would have been much longer, only if I could have spent slightly more time in the lab.

I like to thank my lifelong friend, Sara Mingu, for existing.

And finally, my deepest gratitude goes to Ibe Deturck. There is so much to say, yet too little space left. I will always be grateful that you entered my life and turned it into a heaven. You were next to me every second of this work for the entire quarantine period, and I hope you will still be there when life goes back to normal. Thank you, for eternity…

ABSTRACT

Blood Brain Barrier (BBB) is one of the main constituents of the central nervous system that differs from non-brain endothelial vessels by its strictly controlled integrity and selective permeability. The loss of BBB integrity has been found to be related to the major neurodegenerative diseases including Alzheimer's disease, Parkinson's disease and multiple sclerosis. In order to understand the underlying molecular mechanisms of these diseases, to develop new treatments and to test possible drug candidates, it is an urgent need to develop a platform that allows the easy tuning of the permeability of the endothelial layer. BBB-on-a-chip is a microfluidic device that is of increasing interest in the last decade and studies focus on the achievement of most physiologically relevant permeability of the endothelial cell layer. The use of pulsed electric field (PEF) for the BBB permeability tuning grants significant advantages over the previously tested methods; parameters of the electric field such as the amplitude, frequency, pulse duration and pulse number can easily be changed during the experiment, the application can be automatized and programmed, electric field can be applied to entire cell layer or it can be focused on specific regions and most importantly, paracellular and transcellular permeability can be induced separately. In this thesis, the possible effects of the induced electric field were investigated by the Finite Element Method (FEM)-based simulations. Two main configurations of BBB-on-a-chip, namely single-layer and multilayer chip, were modelled as 3D-constructs and the distribution of the potential, electric field and current density were simulated for different frequencies. Possibility of paracellular and/or transcellular permeabilization were discussed for different frequency regions. Accordingly, multi-layer chip configuration was found to have several major disadvantages for the use of electric field for permeabilization purposes.

TABLE OF CONTENTS

LIST OF FIGURES

LIST OF TABLES

1 INTRODUCTION

1.1 Biology of Blood-Brain Barrier and the Tight Junctions

Major brain tasks, such as sensation, memory and motion, and underlying homeostasis, synapse activity and processing of information, require the precise distribution of metabolite and oxygen through the cerebral blood vessels (Zlokovic, 2011; Blinder et al., 2013; Andreone et al., 2015). This precise distribution and delivery require the collective and coordinated activity of several central nervous system (CNS) elements; neurons, vascular cells such as pericytes and endothelial cells and glial cells such as astrocytes.

Among these, endothelial cells constitute one of the most striking features of the CNS; the blood-brain barrier (BBB), which serves to restrict the entry of wide variety of component, including toxins, pathogens and blood cells (Winkler et al., 2011). The transport of essential proteins, metabolites and nutrients into the brain and the export of metabolic waste products from interstitial fluid (ISF) back into the blood is strictly regulated by substrate specific transport proteins or protein complexes on the endothelial membrane of the BBB.

Endothelial monolayer constituting the BBB differs greatly from the blood vessels throughout the rest of the organism due to the presence of important CNS cells and extracellular matrix components regulating not only its formation but also its maintenance, strength and permeability. Unlike non-brain endothelial layers, BBB exhibits i) significantly low non-specific pinocytosis and prevents the paracellular diffusion of most hydrophilic compounds, ii) strong asymmetric distribution of transporters on two sides of the monolayer for the protection of upmost important brain homeostasis, and iii) it requires a larger amount of mitochondria to support the high demand of metabolic activity. Altogether, this results in low barrier permability and so high trans-endothelial electrical resistance (TEER) (Brightman & Kadota, 1993; Petty & Lo, 2002; Abbott et al., 2006).

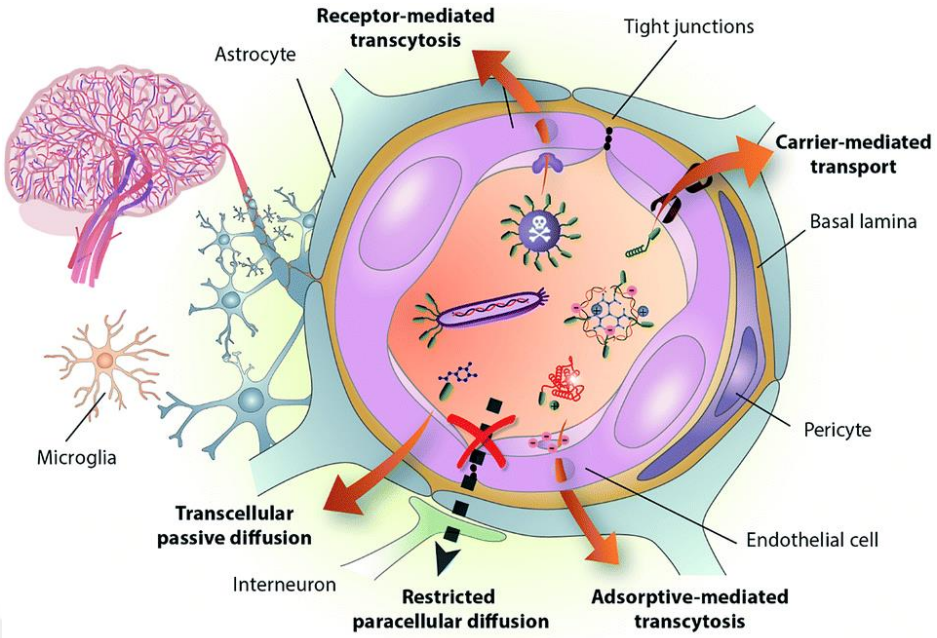

Figure 1.1. Representation of the constituent of and the major transport events over the Brain Blood Barrier (Oller-Salvia et al., 2016).

The basal lamina of the BBB is composed of three main layers (Fig. 1.1), an external layer containing mostly laminin-I and laminin-II produced from glial cells (mostly astrocytes), an internal layer containing laminin-IV and laminin-V produced directly from the endothelial cells and a middle layer that contains collagen IV that is contributed from both glial and endothelial cells (Perlmutter & Chui, 1990). Matrix metalloproteases and Tissue Inhibitor of Metalloproteases (TIMPs) are responsible for most of the regulation of BBB integrity both for the healthy homeostasis and the inflammatory conditions (Yong, 2005). Even though the exact mechanism of glial cell-mediated BBB regulation remains to be uncovered, several extracellular proteins produced by astrocytes, including neurotrophic factors, angiotensin-II and angiopoietin-I, are shown to be required for the maintenance of the BBB integrity and its extremely low paracellular permeability (Lee et al., 2003; Hoti et al., 2004; Wosik et al., 2007). Similarly pericytes, which are also found in non-brain endothelial layers but to a lesser extent, were shown to be directly correlated with the vasoregulation and low permeability of the BBB in the brain (Lindahl et al., 1997; Peppiatt et al., 2006).

Even though the regulation and the number of factors involving in the tight junction of endothelial cells in the brain are strongly different from their non-brain counterparts, the structural constitution of the tight junctions in the BBB is still governed by the similar protein families that form the epithelial tight junctions. Out of these, junction associated molecules

(JAMs), occludins and claudins represent the three main transmembrane proteins that bind two adjacent endothelial cell membranes together. On the other hand, Zonula Occludens, with ZO-I being the most prominent one, represents the direct bridge between these outer proteins and the cytoskeleton of the endothelial cells (Wolburg & Lippoldt, 2002). Regardless of the similarity of the protein families, the specific proteins which take part in BBB still differ from non-brain epithelial layers; for instance tight junctions in BBB were found to express mainly claudin-III and V (Liebner et al., 2000) while the epithelial tight junction are mainly composed of claudin-I, II and XI (Wolburg et al., 2001). Resembling the non-brain equivalent, BBB tight junctions are also strongly regulated by several signaling pathways, of which the cAMP pathway is shown to be the main regulator where the phosphorylation of the structural proteins that belong to the Zonula Occludens and occludin family directly translates into the strength of tight junctions (Levanony et al., 1992). It has been shown that phosphorylation of ZO-I is related to the increase of permeability, while the phosphorylation of the occludin decreases the paracellular permeability of the BBB (Rubin, 1992; Yamamoto et al., 2008). Likewise, other signaling proteins such as VEGF, GTPases, ICAM-I and reactive oxygen species (ROS) have shown to take part in the integrity of the tight junctions, either directly or indirectly by affecting the actin cytoskeleton (Jou et al., 1998; Schreibelt et al., 2007).

Overall, BBB is one of the most essential structures for the brain activity, due to its highly regulated tight junctions, that is responsible for the strict control of the transport of molecules between the body and the brain, for the prevention of the diffusion of harmful substances, adequate supply of important metabolites and nutrients, the efflux of metabolic wastes and for the regulation of trans-endothelial transport of circulating immune cells and inflammatory factors, all of which are factors required for the accurate brain homeostasis and activity. Hence, it is no surprise that many CNS-related diseases, including but not limited to Alzheimer's disease, Parkinson's disease, brain injury, ischemic stroke, epilepsy, multiple sclerosis (MS) and also psychiatric disorders such as major depression and psychosis were all found to be directly or indirectly related to the BBB dysfunction, either as the cause or the result (Abbott et al., 2006; Abbott et al., 2010).

This requires the complete understanding of the regulations of BBB under different physiological conditions for a deeper understanding of certain neurodegenerative diseases and drug delivery to the brain. Even though *in vivo* studies provide valuable findings, these experiments suffer from the qualitative data they provide and no direct translation to human tissue equivalents, along with other well-known issues such as being labor-intensive,

significantly costly and ethically controversial. For this reason, microphysiological *in vitro* BBB models represent a significant importance for the initial phase of the drug development process that not only saves time and money, but also helps the development of a correct drug candidate for a given specific disease condition. Hence, most of the papers published on *in vitro* BBB studies focuses on the optimization and the maintenance of the permeability of endothelial layer with an easily repeatable and adaptable experimental design and construct.

1.2 Current approaches on BBB-on-a-chip

Even though most of the *in vitro* BBB studies rely on the use of Transwell or other two-chamber large constructs (Fig. 2a). This technique suffers from significant drawbacks such as the lack of direct incorporation of sensors and real-time readouts, lack of possibility to study other important BBB functions than just permeability, such as leukocyte extravasation or signaling processes and the inconvenience of growing more than two cells simultaneously (Van der Helm et al., 2016). For these reasons and more, there has been an increasing interest on finding other solutions with the help of emerging micro-nano technology and fabrication techniques, especially in last decade. BBB-on-a-chip represents a superior alternative to Transwell assays due to its high versatility, repeatability, rapid and even automated analysis and relatively low-cost design. These are small microfluidic devices with tiny networks of microchannels and chambers where the desired cells are seeded, and corresponding tissues are mimicked by the supply of physiological fluids and the restricted geometry. Depending on the parameters used in the BBB-on-a-chip, such as the mechanical factors, accessory cell types, extracellular metric and the geometry, the desired physiological conditions can be introduced in a controllable fashion to better mimic of different diseases to study underlying molecular mechanism, to investigate the effect of existing or developing therapies or to test different drug candidates.

However, being at the early stages of research, BBB-on-a-chip still lacks the complete representation of the *in vivo* conditions and integrated read-out systems are still not fully optimized for the easy use to obtain a reliable, and more importantly, consistent results. In fact, up to 2016, barely ten publications on BBB-on-a-chip were issued in literature, among which only two used human originated brain endothelial cells. Even though the number of publications is increasing fast after these initial set-up studies, construction of the chips, established conditions and the resulting data still differs significantly between each study, creates a major inconsistency among the studies, even when the objective is completely the same.

Even though the complete geometry can differ greatly between each study, there are three main structural approaches to grow endothelial cells on a BBB-on-a-chip. In a multi-layer configuration (also called stacked or vertical) (Fig. 2b), one channel to accommodate endothelial monolayer (aka. BBB channel) is separated physically by a porous membrane from the other channel that will contain either solely culture media or other important cells such as pericytes and astrocytes (aka. Brain chamber) (Booth & Kim, 2012; Griep et al., 2013; Achyuta et al., 2013; Brown et al., 2015; Walter et al., 2016). This approach, however, lacks from several drawbacks such as difficulties for direct observation of cell culture and problems with the assembly of different chip components that are fabricated separately where any mismatch between layers can induce the leakage from the channels.

In order to achieve easier fabrication, handling and better inspection with microscopy, single-layer (also called flanked or lateral) BBB-on-a-chip is preferred (Fig. 2c). In this approach, one or two BBB-channels and usually a single brain chamber are fabricated next to each other on a single layer (Deosarkar et al., 2015; Xu et al., 2016; Partyka et al., 2017). Instead of using a porous polymer membrane, PDMS pillar or stacks are fabricated between two components where the endothelial cells can attach and fully form the BBB monolayer. In order to fully separate two components, hydrogels can also be introduced in either component that not only gives a 3D structure for the growth of cells but also prevents the cells belonging to other components to enter the hydrogel-containing chamber, while still permitting full communication between the channels.

Both of these techniques, at the end, hosts an endothelial layer that is planar (2D), either located on top of the polymer membrane or located vertically between the PDMS stacks. For the full mimicry of the *in vivo* BBB structure, there is an increasing number of studies trying to produce tubular structures where the endothelial cells are expected to attach on the surface of the hollow fiber-like scaffold which will be removed as a sacrificial layer (Fig. 2d) (Herland et al., 2016; Marino et al., 2018; Linville et al., 2019). However, given that the fabrication and handling is more complicated, this approach is still not well characterized and far from common use in research.

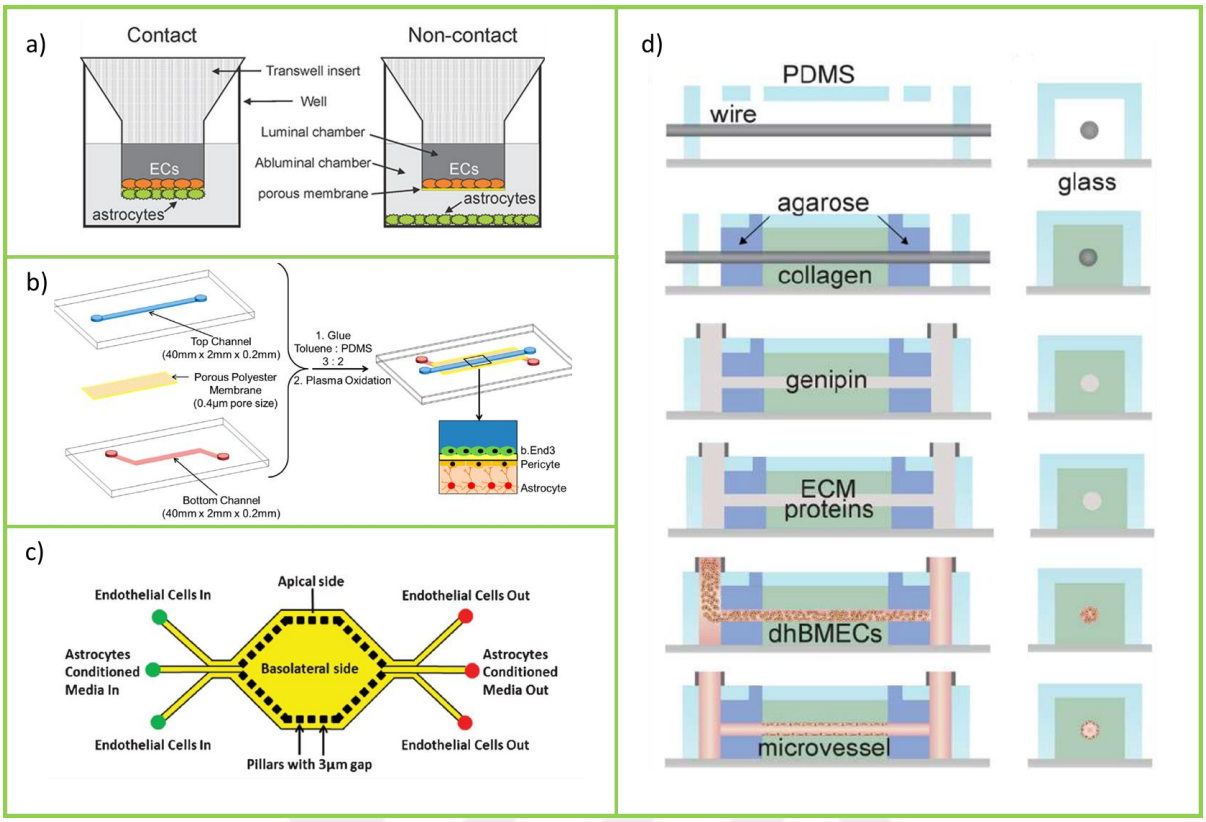

Figure 1.2. Common in vitro Blood-Brain Barrier models. a) the regular Transwell model for direct contact and indirect contact between endothelial cells and astrocytes (Niego & Medcalf, 2013) b) multi-layer structure with porous membrane between the layers (Wang et al., 2006) c) single-layer structure with PDMS pillars between the layers (Prabhakarpandian et al., 2012) d) tubular structure (Linville et al., 2019)

1.3 Characterization of BBB-on-a-chip permeability

Regardless of the geometry of the structure, almost in all of the cases, the inconsistencies lie on the resulting permeability of the endothelial monolayer, which is measured either manually by fluorescent tracking of transported species, or more recently by the use of electrodes to measure the electrical resistance across the endothelial monolayer. TEER is one of the widely used techniques for the quantitative analysis of barrier integrity and permeability and it can also be used in other systems to follow the cell behavior such as proliferation and migration (Srinivasan et al., 2015; Henry et al., 2017). *In vivo* TEER measurements reveal that the resistance across BBB can change approximately between 1500 and 8000 $\Omega.cm^2$ depending on the health condition, age and other factors (Wolff et al., 2015). Hence, it is important to obtain a TEER value in this range in BBB-on-a-chip applications before proceeding to the main objective of the study. Unfortunately, many studies fail to fall in this range of electrical resistance, and

therefore the desired permeability observed in physiological conditions, mainly because of different parameters used in chip fabrication and different ways of obtaining TEER. TEER can be obtained either by measuring the resistance by Ohm's law, which ignores many important biological factors affecting the permeability, or by the analysis of impedance across a range of frequencies, which considers not only resistive but also capacitive and inductive contributions, and after an initial analysis, it reveals the most optimal single-frequency to be used for the following TEER measurement (Bard and Faulkner, 2000). After the impedance spectrum is obtained, the data are fit to an electrical circuit equivalent by the least-square optimization method in order to obtain factors contributing to impedance separately, such as double layer capacitance of the electrodes that are used for TEER measurement, resistance of the culture medium, and resistance and capacitance of the endothelial monolayer (Elbrecht et al., 2016). In order to avoid electrode polarization and the variations of cell culture medium resistance, instead of using 2 probes, the 4-probe approach is recommended (Van der Helm et al., 2016), where two electrodes are used to deliver current and the other two electrodes are used to measure voltage, or vice versa. There are several major factors affecting the resulting TEER, among which the presence of pericytes/astrocytes, shear stress, the distance of the electrode from the cell monolayer, position, shape and orientation of the electrodes with respect to endothelial cells (to generate a uniform electric field), conductivity of the electrolyte inside the microfluidic chips, the presence of other resistive materials inside the chips (i.e. porous membrane and PDMS) and the type of electrode material are all shown to result in major variations in TEER measurements (reviewed in Mir et al., 2020, submitted manuscript).

1.4 Tuning Permeability of the BBB-on-a-chip

As explained earlier, the breakdown of the BBB integrity and corresponding increase of permeability have been observed in many neurodegenerative diseases including multiple sclerosis, Parkinson's and Alzheimer's (Fu, 2012). Studying the molecular basis of these diseases and developing new therapies requires the ability to control the permeability of endothelial monolayer *in vitro*. Moreover, while essential for the brain function, the integrity of the BBB also limits the success of therapies by preventing the drug transport into the brain. Delivery of drugs into the brain can be achieved by either the transcellular pathway; through the cell or paracellular pathway; in between the cells. In a normal functioning BBB, the tight junctions prevent the passage of hydrophilic molecules that have a larger molecular weight than approximately 500 Da (Fu, 2012). On the other hand, transcellular transport is strictly controlled for the passage of only specific proteins and it restricts the passage of most of lipophilic, large

drugs for CNS treatment (Santaguida et al., 2006). All these limitations highlight a requirement for the manipulation and tuning of the permeability both *in vivo*, for the better delivery of the drug particles, and *in vitro*, for the drug development and drug permeability studies along with a better representation of the specific pathological conditions with corresponding physiological BBB permeability.

Several techniques have been investigated to temporarily increase the permeability of BBB both *in vivo* and *in vitro*, including the use of chemicals, osmotic pressure, focused ultrasound and electric field, all of which present advantages and disadvantages (Warren et al., 2006, Kroll et al., 1998; Hynynen et al., 2005; Arena et al., 2014; Garcia et al., 2012). Chemical or pharmaceutical treatment is usually the least favored method as it may have systemic effects on the rest of the CNS cells which lead to several side effects such as abnormal neuron function, nausea and headache *in vivo* (Treat et al., 2007) and it can change the behavior of not only the endothelial cells but also the supporting cells such as pericytes and astrocytes *in vitro*. Delivery of drugs in theory can be aided with osmotic opening. However, it is not yet possible to control and tune the extent of cell shrinkage and the resulting permeability by this technique (Kroll et al., 1998). Focused ultrasound, although is noninvasive and mostly safe, it has a very restructured coverage area that limits the permeability tuning to a small part of the BBB and leads to extended treatment period once larger volumes of BBB is required to be permeabilized (Liu et al., 2010). A more recent approach to temporarily increase the permeability of BBB is the pulsed-electric field (PEF) treatment that has several major advantages over the previously mentioned methods. PEFs are intense, short electric fields that have already been used clinically for the treatment of several CNS pathologies, including deep-brain stimulation (DBS), electroporation, electrochemotherapy and tumor treating fields (Vitek, 2008; Agerholm-Larsen et al., 2011; Davalos et al., 2005). The main advantage of using PEF comes from the fact that depending on the easily adjustable parameters used such as the magnitude of electric field, number of pulses, duration of the pulse, polarization and the frequency, PEF can be used to administer both transcellular and paracellular permeability in BBB, both *in vivo* and *in vitro*, without causing little to no harm to surrounding tissues and cells (Lopez-Quintero et al., 2010; Arena et al., 2014). While the effects of PEF on transcellular permeabilization are well established, the mechanism of action of PEF on paracellular permeability of the BBB still remains ambiguous.

Transcellular permeability can be increased by inducing electroporation by PEFs, which causes transmembrane potential over the endothelial cells to exceed a certain threshold and induce the

formation of nanoscale aqueous pores on the membrane (Kotnik et al., 2010). Depending on the ability of the membrane to reseal these pores, electroporation can be either reversible or irreversible (IRE). Considering the IRE eventually results in the death of the corresponding cell, it is important to establish the extent of reversible electroporation and the threshold of IRE in order to avoid endothelial apoptosis while still increasing the transcellular permeability of the barrier.

1.5 PEF induced BBB Permeabilization in literature

One of the earliest studies on the reversible and IRE effects of a low magnitude electric field on BBB integrity came from Garcia et al. (2012), where the electroporation has shown to be reversible at electric fields below 400 V/cm where the temporary BBB permeability increase occurs *in vivo*. Similarly, Hjouj et al. (2012) also studies the thresholds for reversible and irreversible electroporation of BBB in rats and found that a temporary permeability increase without significant cell death occurs between 330 V/cm and 500 V/cm at 4 Hz with pulse duration of 50-70 μs. Arena et al. (2014) showed that *in vivo* BBB permeability increases without irreversible electroporation at much lower electric field amplitudes, 200 pulses of 250 V/cm with only 850 ns pulse duration.

Even though above mentioned and other *in vivo* studies provide valuable information about the reversible BBB permeabilization, these results remain mostly qualitative and cannot cover all the parameters that can be adjusted for PEFs and investigated throughout. On the other hand, *in vitro* assays not only save a great amount of time and cost, but also provide more quantitative results where the distinction between the results of different PEF-induced BBB permeabilization can be clearly demonstrated. Moreover, as explained earlier, it is important to obtain an optimized *in vitro* BBB platform with controllable permeability for the study of new treatments and to test new drug candidates. For this reason, the observation of the effect of PEF on endothelial cells *in vitro* has gained major interest during the last decade.

One of the earliest *in vitro* studies on the electric field induced barrier permeabilization came from Lopez-Quintero et al. (2010), where the authors investigated the effects of DBS-relevant, low intensity electric field on the bovine aortic endothelial cells seeded in Transwell. After the estimation of the relevant electric field of DBS near the endothelial cells by the use of the finite element method, 0.62, 1.25 and 2.5 V/cm electric field with 90 μs pulse duration is applied at relatively high frequency of 200 Hz. After the stimulation with PEF, the permeability of the endothelial barrier is assessed by the water flux across the monolayer. Cell viability and calcein

uptake analyses revealed neither reversible nor irreversible electroporation occurred in the electric fields tested. Out of three EFs, 1.25 and 2.5 V/cm resulted in a significant increase of water flux through the barrier, proving the DBS-relevant, low intensity electric fields can induce permeability increase in the endothelial barrier. As these electric fields are well below the typical electroporation threshold, the authors suggested the mechanism of permeability increase might be due to the disruption of the tight junctions. Authors showed that the increase of hydraulic permeability correlated to ZO-1 disorganization. As the effects of the electric field on the tight junction proteins were already known (Shen et al, Bolton et al), authors proposed that even as low as 1.25 V/cm electric fields can induce changes on the tight junction proteins and cytoskeleton to reduce the tight junction strength. Considering that the induced chemical imbalance over the cell results in alteration of the signaling pathways and can eventually lead to apoptosis, even when the electroporation is completely reversible, it was a major finding that the PEFs may still lead to a significant permeability increase without inducing any pores on the membrane of endothelial cells. This evoked new research focus on the paracellular permeabilization of the *in vitro* BBB by the use of electric field.

In order to understand the thresholds of reversible and irreversible electroporation and the underlying molecular mechanisms *in vitro*, Meulenberg et al. (2012) studied a larger window of electric fields between 68 and 685 V/cm at 1 Hz and 8 pulses with a pulse length of 100 μs. Starting from approximately 100 V/cm, the PI fluorescent uptake into cells increases, which indicates the formation of pores. However, this effect was mostly prominent about approximately 400 V/cm. Fluorescein conjugated phalloidin staining showed that F-actin fibers were not affected below 275 V/cm but became less rigid and fragmented with higher electric field values. Similarly, above 275 V/cm beta-tubulins became denser as the cells shrank and collapsed. Also, the survival rate was given as only 31% for the largest electric field applied (685 V/cm), which suggests that the occurrence of irreversible polarization increases quickly within this given range of electric fields. Even though the authors were successful with the determination of the electroporation threshold in their particular Transwell choice, the permeability below the electroporation limit and hence the possibility of paracellular permeability is not investigated and the experiments are conducted on the absence of neuronal cells and the shear stress, which would otherwise increase the electroporation threshold even more.

Zhou et al. (2013), on the other hand, use of the brain microvascular endothelial cells (BMVEC) and the astrocytes co-culture on Transwell constructs for the investigation of the electric field

on the BBB barrier by employing TEER measurements for the continuous track of the paracellular permeability. However, the electric field used in this study was significantly large (1000-4000 V/cm) and not relevant for the threshold between the paracellular and transcellular permeability pathways.

Bonakdar et al. (2016) studied the effects of the electric field on BBB-on-a-chip for the first time by using microfluidics. In this initial study, the authors focused on electroporation relevant electric fields gradually changing between 214 (at the edges of the microchannel) and 714 V/cm (at the middle of the microchannel) and employed three different pulse number (10, 30 and 90) with a pulse duration of 100 μs at 1 Hz. Even though the experimental construct lacks the astrocytes/pericytes and shear stress, the authors clearly demonstrated that the lower pulse number (10) and low electric fields (until 580 V/cm) resulted in a relatively safe electroporation while the occurrence of irreversible electroporation and the corresponding cell death was significantly larger for 30 and 90 at even smaller electric fields. This study clearly shows that the number of pulses for PEF induced BBB permeabilization is as important as the magnitude of the electric field used. The study of the paracellular permeability by using electric fields much lower than the electroporation threshold was left for the following study from the same group, where the exact electric fields used in Lopez-Quintero et al. (2010) were tested and compared to a larger electric field (Bonakdar et al., 2017). Even though the experimental design suffered from the same drawbacks of the previous study, the authors improved the design of Lopez-Quintero greatly by using multilayer BBB-on-a-chip model with a uniform electric field density and measuring the permeability of both fluorescent sodium salt (376 Da) and FITC-Dextran (70 kDa), instead of hydraulic permeability, in order to understand the transport of small and large molecules. Accordingly, permeability to a small molecule increases even at extremely low electric field at 2.5 V/cm while the permeability to a large molecule increases only at 25 V/cm. Considering these electric fields were far below the threshold of electroporation, the authors proposed that the paracellular permeability increases in this range of the electric field, yet this theory is left to be addressed in the future.

One of the latest studies on this subject was conducted by Sharabi et al. (2019) where the authors included the pericytes in Transwell configuration to enhance the tight junction expression on adjacent endothelial cells and the impedance spectrum-based TEER measurements to carefully examine the permeability changes, while no shear stress is induced on the cells. Both low voltage regime between 5 and 100 V (approximately 7 and 150 V/cm) and high voltage regime between 200 and 2000 V (approximately 300 and 3000 V/cm) at 1 Hz, 10 pulses with a pulse

duration of 50 μs, were tested for viability, electroporation and permeability measurements. Accordingly, no significant cell death is found below 100 V, suggesting no irreversible electroporation. Endogenous lactate dehydrogenase (LDH) release experiments revealed the electroporation starts only after 100 V while the permeability to Sodium Fluoresceoin (NaF) increased almost 40% even at 10 V, suggesting that the electroporation was not the reason for permeabilization in these low electric field regimes. This result is supported by a significant decrease in TEER after the application of PEF at 10 V (no TEER change is obtained for 5 V). These findings were tried to be confirmed by ZO-1 and VE-cadherin immunostaining, however, the confocal microscopy analysis did not correlate to the previous results. Once again, the mechanism of action of BBB disruption at low PEFs was left to be elucidated in the future.

Table 1. Summary of the recent studies on the pulsed electric field induced permeability change in BBB in vitro models

REFERENCE	*ELECTRIC FIELD (V/cm)*	*PULSE DURATION (μs)*	*PULSE NUMBER*	*FREQUENCY (Hz)*	*PROS*	*CONS*
LOPEZ-QUINTERO et al. (2010)	0.62 1.25 2.5	90	Continuous	200	ZO-1 Immunostaining	TransWell No permeability assay No TEER. No Shear stress No astrocytes/pericytes.
MEULENBERG et al. (2012)	68, 137, 274, 411, 548, 685	100	8	1	Actin/Tubulin immunostaining	TransWell No shear No astrocytes/pericytes No TEER.
BONAKDAR et al. (2016)	214 to 714	100	10 30 90	1	Microfluidics	Only high EFs addressed No immunostaining No TEER No Shear stress No astrocytes/pericytes
BONAKDAR et al. (2017)	2.5 25	10	Continuous	200	Microfluidics	No TEER No Shear stress No astrocytes/pericytes No immunostaining
SHARABI et al. (2019)	7 to 147	50	10	1	Pericytes TEER	TransWell No astrocytes No consistency in immunostaining findings

PEF induced BBB permeabilization is a very relevant technology yet still in its infancy. More comprehensive research is required for the fully understanding of this technique and many important factors expected in a physiologically relevant *in vitro* model still not considered in these studies, such as the human brain endothelial cells, neural cells such as astrocytes and pericytes and shear stress.

1.6 The Aim of the Present Study

There has been no research carried out that both mimics the BBB conditions and studies the effects of a low electric field on paracellular permeability comprehensively, nor any research to explain the findings of above-mentioned pioneering studies. Considering the importance of being able to manipulate the permeability of BBB for improved drug delivery or for the reconstruction of disease-induced permeability increase in brain capillaries, it is an urgent need to develop a realistic BBB-on-a-chip that allows measuring the effects of varying PEFs on tight junction structures in both molecular and physiochemical levels.

In this study, the effects of the applied electric field on the cell layer by the integrated electrodes in two main configurations of BBB-on-a-chip; single-layer and multilayer, were investigated by 3D modeling. Due to COVID-19 pandemic, the study was restricted only to finite-element analysis based simulations and the theoretical calculations where the underlying effects of the electric field was investigated by considering the physical parameters, such as conductivity, relative permittivity and the geometry of the structural elements in the corresponding chip configuration. The detailed analysis of the potential, electric field and the current density distributions over the constructed endothelial layer was carried out to explain the possible outcomes of the use of electric field. Finally, the advantages and the disadvantages of both chip configurations were discussed with respect to their use in PEF-induced permeability tuning studies.

2 METHOD

2.1 Numerical Modelling and Parameter Settings

For the comparison of two different chip designs with respect to the potential, electric field and current density distribution over the cell layer, finite element simulations were modeled in COMSOL Multiphysics 5.2 (Stockholm, Sweden) using the AC/DC module with the frequency-dependent study. Electric Currents physics was chosen to solve the following equations to obtain the distribution of electrical parameters such as potential (V), induced electric field (**E**) and the current density (***J***) on different structural domains;

$$\boldsymbol{J} = \left(\sigma + \epsilon\frac{\partial}{\partial t}\right)E$$

with the boundary condition of $\nabla.\boldsymbol{J} = 0$

$$\nabla \text{ x } \left(\frac{\mu_0}{\mu}\nabla \text{ x } \mathbf{E}\right) - \omega^2\epsilon\mu_0\boldsymbol{E} = 0$$

where $\epsilon = \epsilon_r \text{ x } \epsilon_0$ and $\mu = \mu_r \text{ x } \mu_0$ with ϵ_r and μ_r are the relative permittivity and relative permeability, respectively.

The boundary condition of the study was introduced as two fixed potentials at electrode boundaries;

$$V_{front\ electrode} - V_{back\ electrode} = Vcos\omega t$$

where V is the externally applied driving voltage and ω is the chosen frequency (1 Hz for the fixed frequency studies and 1 kHz-1 GHz for the frequency sweep studies). The remaining boundaries were defined as electrically insulating, i.e., $\boldsymbol{n}.\boldsymbol{J} = 0$; where $\boldsymbol{n}$ is the normal vector to the surface.

The electrical parameters of the structural domains are given in Table 2. The values of the parameters as the average of previous similar studies (Sano et al., 2014; Taghian et al., 2015; Murovec et al., 2016; Jayasooriya & Nawarathna, 2017; Li et al., 2018).

Table 2. Conductivity and permittivity parameters used for the structural elements in 3D Model

Parameter	***Value***
Channel/Chamber conductivity (σ_{PBS})	*1.6 S/m*
Channel/Chamber permittivity (ϵ_{PBS})	*$80\epsilon_0$*
Cell membrane conductivity (σ_m)	*10^{-7} S/m*
Cell membrane permittivity (ϵ_m)	*$7\epsilon_0$*
Cytoplasm conductivity(σ_c)	*1 S/m*
Cytoplasm permittivity (ϵ_c)	*$80\epsilon_0$*
Polycarbonate conductivity (σ_{PC})	*10^{-14} S/m*
Polycarbonate permittivity (ϵ_{PC})	*$3\epsilon_0$*
Pillar conductivity (σ_{PDMS})	*2.5×10^{-14} S/m*
Pillar permittivity (ϵ_{PDMS})	*2.75*

At the beginning of each simulation, four different built-in physics-controlled meshing were carried out; normal, fine, finer and extremely fine. In each scenario, only the extremely fine mesh gave the results expected by theoretical calculations. This was confirmed by the color images of mesh quality where any mesh below extremely fine resulted in low-quality mesh elements where the small structural features are located. For this reason, an extremely fine mesh with free tetrahedral mesh elements was created before the corresponding simulation was run for all the following studies. In case of chip structures with the cell layer, additional Edge and Free Triangular nodes were used for the better meshing of the small edges and the small boundaries, respectively.

The construction and the corresponding geometry of the structural domains are given in the following sections. All simulations were repeated for the chip designs without the cell layer (control) and with the cell layer.

2.2 Design and Optimization of the Single-Layer Chip Design

A 3D lateral chip was constructed by the 150 μm extrusion of a 7700 μm x 1900 μm rectangle to accommodate 19 pairs of PDMS pillars that are separated by 100 μm between their longest edges (Fig. 2.1). The edges of PDMS pillars were chosen as 300 μm for the outer edge, 200 μm for the size edges and 70 μm for the inner edge. Throughout the following simulations, pillars were assigned PDMS with a conductivity of 2.5×10^{-14} and relative permittivity of 2.75. Regions of the single-layer chip outside of the pillars was assigned water with a modified conductivity of 1.6 S/m and relative permittivity of 80 to represent the physiological parameters of PBS.

The electrodes were constructed as 2D circular disks and assigned gold as material. Unless mentioned otherwise, the centers of the 2D electrodes were kept 150 μm before (x=150) and after (x=450) the gap between two pillars, where the endothelial cells are expected to form. To be able to manipulate the cell layer, both by using a group of electrodes and also individually in the same chip construct, four pairs of electrodes were placed in the first four gaps between the pillars; following two gaps were left empty and the next three pairs of electrodes were placed with one empty gap between them. No electrode was introduced between the upper pillars to have endothelial cells that are not exposed to an electric field in in the same chip design during the experimentation.

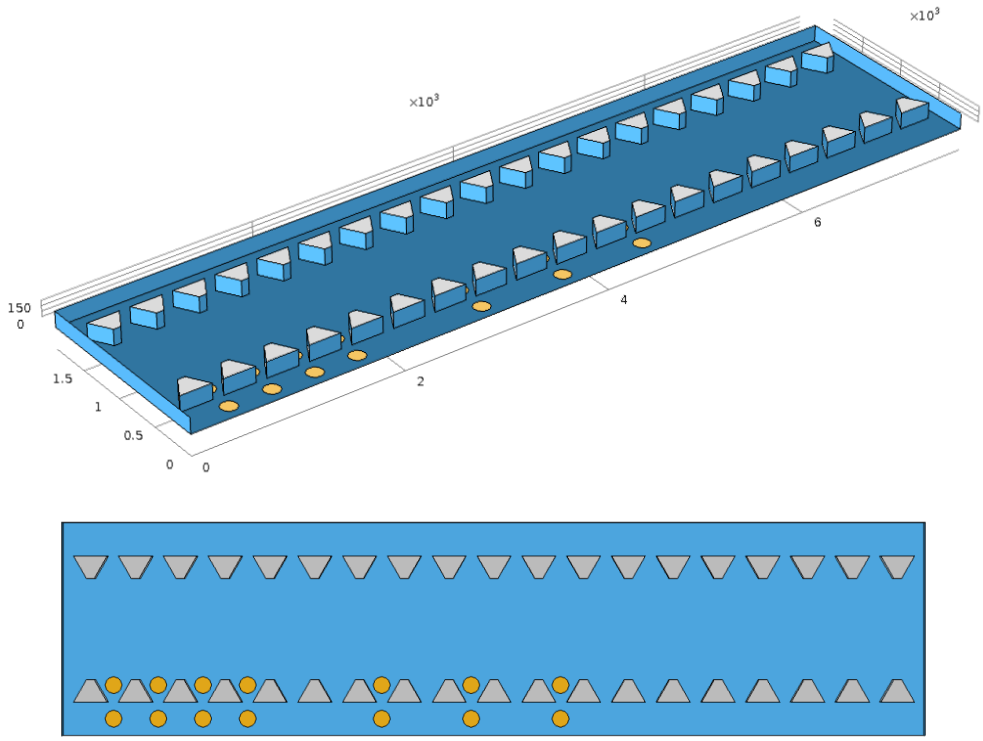

Figure 2.1. Final structure of the single-layer chip design before the cell layer is introduced (121,852 mesh elements with a minimum element size of 1.54 μm)

For the studies involved in the optimization of the single-layer chip, three main cutlines were chosen to be analyzed. One cutline of approximately 6000 μm length was taken as passing along the long axis of the chip, located just at the base of the pillars in order to see the difference of electric field in each of the gaps in a single graph (Fig. 2.2, red line). A second cutline of 300 μm was taken between the centers of two electrodes located in the second gap (between the second and third pillar) in order to understand the electric field distribution through the individual gap (Fig. 2.2 blue line). A third cutline of 150 μm was taken from the bottom to the top of the chip at the point of the second gap in order to measure the electric field distribution along the height of the chip where the endothelial cells are expected to form a vertical barrier (Fig. 2.2, violet line).

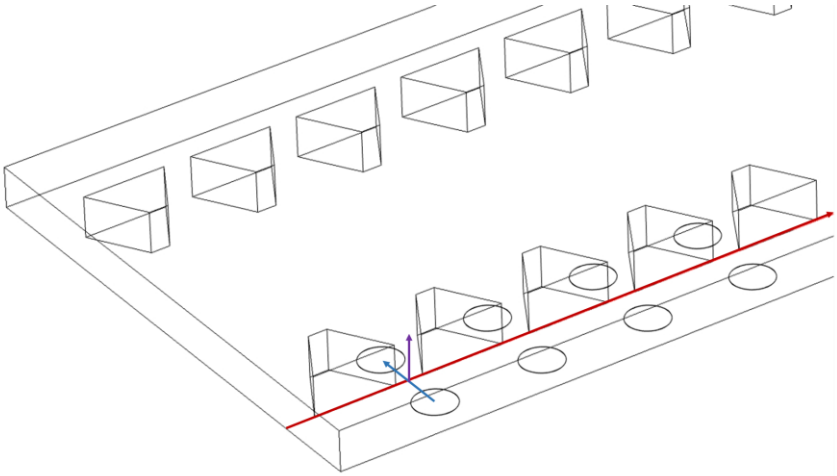

Figure 2.2 Representative image of the three main cutlines used in the single-layer chip analysis. The red arrow represents the cutline along the long axis of the chip; the blue arrow represents the cutline between the centers of two electrodes; the violet arrow represents the cutline along the height of the gap between two pillars.

As for the first step of the optimization, three different diameters of electrodes were tested; 50 μm, 100 μm and 150 μm. Smaller electrodes were not considered to reduce the complications in the alignment of the electrode layer and the PDMS layer during fabrication; similarly, larger electrodes were not considered as they would not fit between two pillars.

The effects of the distance between two electrodes on the electric field distribution along the height of the channel were investigated by using only 50 μm electrodes in order to be able to test larger distances. In this study, the distance between the centers of the electrodes was gradually increased from 300 μm to 1700 μm and results of four chosen distance values were compared.

To check the effect of the electrode paths on the electric field distribution in the gap between the pillars, 70 μm paths were added to all electrodes and extended towards the two opposite sides of the chip (Fig. 2.3a). After the results were obtained, electrode paths were removed and the circular electrodes in the brain chamber were replaced with a single rectangular electrode as shown in Fig. 2.3b.

a)

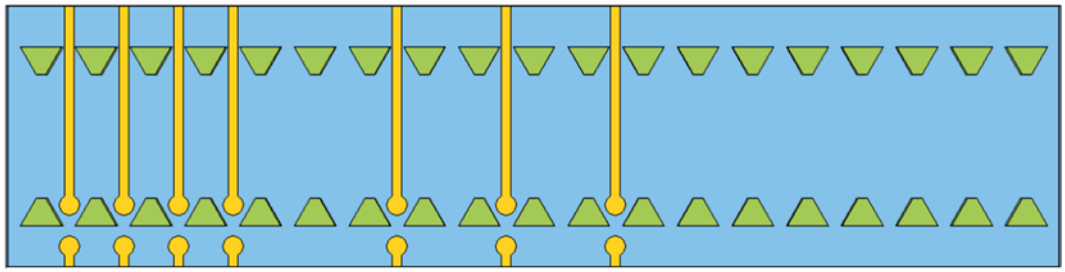

b)

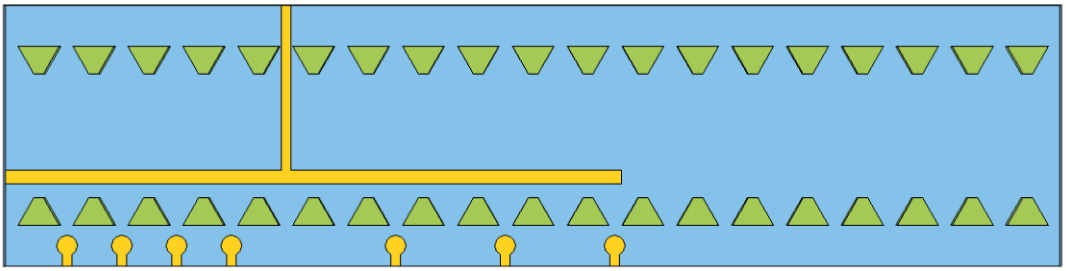

Figure 2.3. Optimization of the single layer chip. Top view of single-layer chip design with a) the electrode paths are introduced and b) electrodes in the brain chamber are replaced with a single rectangular electrode

2.3 Modelling of The Cell Layer in The Single-Layer Configuration

Cellular structures were constructed as one hollow rectangular prism with a certain thickness; representing the cell membrane, surrounding a smaller rectangular prism; representing the cytoplasm. Dimensions of the cell were chosen considering the reported in the literature for endothelial cells in BBB (Farkas and Luiten, 2001; Nicaise et al., 2009) and it was considered to be 50 μm in length, 20 μm in height and 0.5 μm in thickness. On the other hand, in order to prevent the problems with meshing and to decrease the amount of time simulation takes to complete, the thickness of the cell membrane was increased to 50 nm from its physiologically more relevant size of 5-10 nm. For similar purposes, the simulations were confined to a single gap between two pillars and the total size of the chip is reduced accordingly. In total 14 cells were placed between two PDMS pillars with a 10 nm gap between two adjacent cells to represent the tight junctions between endothelial cells in BBB (Fig. 2.4). As there is no study which investigated the conductivity of the human brain endothelial cell membrane to the best of our knowledge, the cellular membrane was assigned to the conductivity of red blood cell

membranes, that is 10^{-7} S/m, and a relative permittivity of 7 to represent the electrically insulator part of the cell. On the other hand, the cytoplasm was given a conductivity of 1 S/m and relative permittivity of 80 to represent the electrically conductive part of the cell.

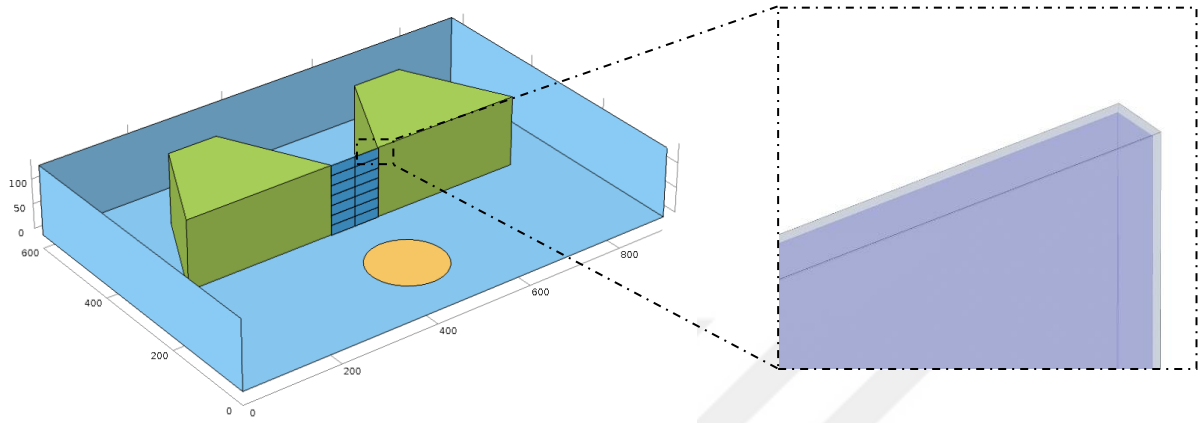

Figure 2.4. Single-layer chip design with 14 cells between two pillars (361,870 mesh elements with a minimum element size of 0.01 μm)

After the introduction of the cell layer, the cutline between the centers of two electrodes was still used to have a general idea of how parameters were distributed in a long range. However, the remaining analyses were carried out for a much shorter cutline in the same direction, extending only between 0.5 μm before and after the cell structure. Together with the 0.5 μm cytoplasm and the 50 nm cell membrane in two sides, the total length of the cutline was only 1.6 μm. It was necessary to look at very short distances once the cell structure was included in order to have enough data points on the small details in the line graphs, such as the behavior inside the cell membrane or the tight junction. If it was still necessary to scale down a particular region to have a clearer picture, even shorter cutlines were used and the results were included as insets. Lastly, another cutline with the same length and direction but passing through the gap between two cells, i.e. tight junction, was analyzed to compare the behavior of the electric field and especially the current density between two important regions.

2.4 Construction of the Multilayered Chip Structure

Unlike the single layer chip design with only one layer of fabrication that contains parallelly two endothelial channels and the brain chamber in between two parallel endothelial channels separated from each other by the presence of the pillars and the endothelial cell layer, the so-

called sandwich design contains three individual layers representing the endothelial channel, the porous membrane and the brain chamber. Only one out of 16 intersection points present in the fabricated chip was constructed for the simulations of multilayer configuration. In order to have 10^5 pores/cm^2 pore density (Cyclopore Track Etched Membrane 7091-4710, Whatman), pores with 1 μm diameters are homogenously distributed inside the polycarbonate membrane with a 32 μm distance between the pores. The area of the membrane, and hence the area of the endothelial channel and the brain chamber, were reduced to 320 x 320 μm from their original size of 2 x 2 mm in order to have a total of 100 pores to run the simulation relatively easier. The length of the endothelial channel and the brain chamber were kept as 180 μm as their original value. Similarly, the length of the porous membrane was kept 10 μm as its original value.

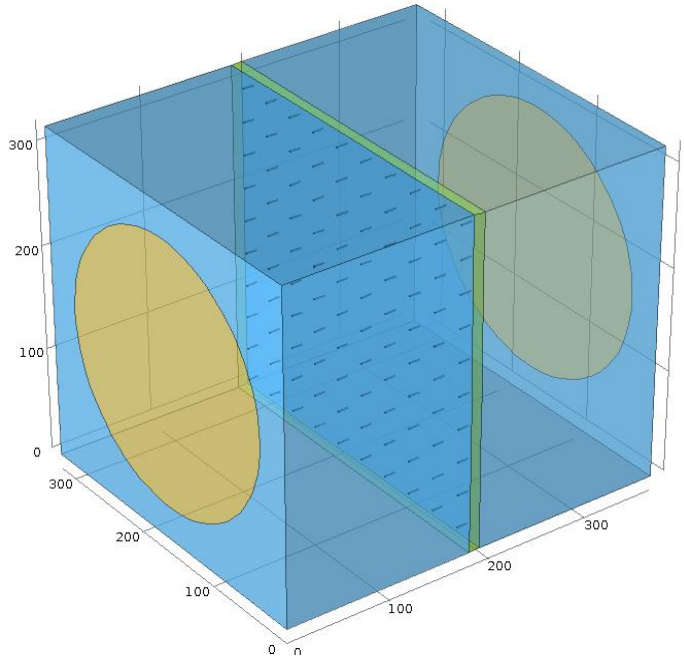

Figure 2.5. Final structure of the multilayer chip design before the introduction of the cell layer (713,208 mesh elements with a minimum element size of 0.1 μm)

To manipulate easier, the layers are placed next to each other rather than being on top of each other, such that the endothelial channel is located on the left, the porous membrane is located in the middle and the brain chamber is located on the right side of the structure (Fig. 2.5). Gold electrodes, whose diameter was reduced to 256 μm from their original value of 1.6 mm, were located on two sides of the structure parallel to the porous membrane. Unlike their original interdigitated structure, electrodes were represented as 2D spherical disks for the sake of easier simulation. Finally, the porous membrane was assigned polycarbonate from the material library

with a conductivity of 10^{-13} S/m and a relative permittivity of 3. The endothelial channel, the brain chamber and the pores were assigned water with the modified conductivity of 1.6 S/m and the relative permittivity of 80.

For the multilayer structure, as the electrodes were placed parallel to the cell layer, electric field was mostly uniform in the direction perpendicular to porous membrane, hence, the analyses were reduced to cutlines in two main directions. One cutline was taken from one electrode to another with a total length of 370 μm and passing through the pore at the middle of the of porous membrane (Fig. 2.6., red line). Another cutline with the same length was taken but this time passing through the polycarbonate region of the membrane close to. Shorter cutlines were also taken to show the porous material in detail and included as insets in the main figures. In order to understand the change of electric field and current distribution between the polycarbonate region and the pores, and to investigate the differences between the edges and the central parts of the porous membrane, a diagonal cutline between one corner of the membrane to the opposite corner, positioned at the middle of the porous membrane, was analyzed (Fig.2.6., blue line). Furthermore, another diagonal cutline was taken 1 μm before the porous membrane in order to understand how the electric field and current behave where the endothelial cells are expected to form the cell layer before reaching their final value inside the porous membrane.

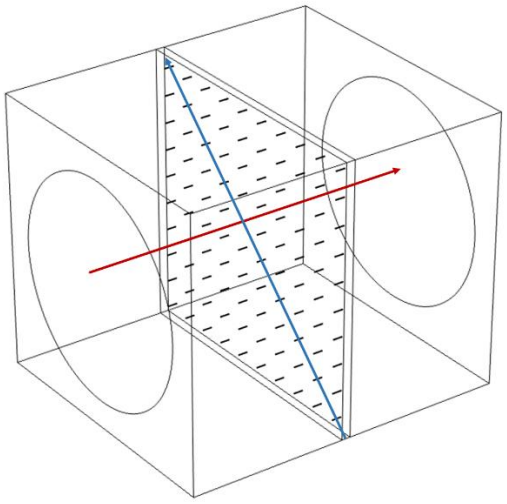

Figure 2.6. Representative image of the two main cutlines and their directions used in the multilayer configuration. The red arrow represents the cutline between the center of two electrodes passing through the porous membrane either through the polycarbonate or the central pore; the blue arrow represents the diagonal cutline between two opposite corners of the porous membrane passing either in the middle of the porous membrane or one micrometer in front of the porous membrane

2.5 Modelling of The Cell Layer in the Multilayer Chip Configuration

Considering the large size difference between the elements in cell construct, such as the membrane thickness and the tight junctions, the size of the multilayer chip was reduced even more to accommodate a total of only nine cells with the same dimensions given before. By keeping the width of the endothelial channel and the brain chamber 180 um, and the porous membrane thickness as 10 μm, the cross-section area of the chip was reduced to 160 x 96 μm (Fig. 2.7). Likewise, the size of the electrodes was reduced to 90 μm such that the electrodes will cover most of the cross-sectional area at two sides of the chip, similar to the original fabricated chip. Cells were placed inside the endothelial channel 10 nm before the porous membrane. Conductivity and relative permittivity values were assigned as explained previously. Finally, the size of the tight junctions between the adjacent cells were kept as 10 nm.

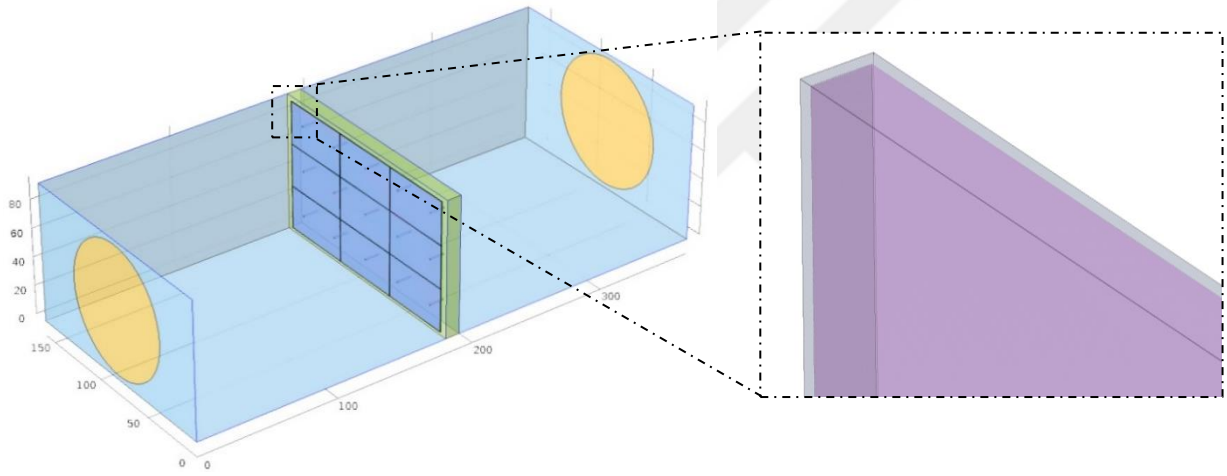

Figure 2.7. Multilayer chip design including nine cell constructs in front of the porous membrane (1,468,141 mesh elements with minimum mesh size of 0.01 μm)

Once the cell layer is constructed in front of the porous membrane, a much smaller cutline between 0.5 μm before and after the cell structure with a total length of 1.6 μm was analyzed. Not only to see the difference between cells and the tight junctions, but also to see the effects of the polycarbonate region of the porous membrane or the pores inside the membrane, three of such cutlines were compared to each other. Accordingly, one cutline was passing through the tight junction followed by the polycarbonate (Fig. 2.8., right image), a second cutline was passing through a cell followed by the polycarbonate (Fig. 2.8., middle image) and a third cutline was passing through a cell followed by a pore (Fig. 2.8., left image). Because of the low porosity of the Whatman paper used in the fabricated chip, it was a low possibility for tight

junctions to be located directly in front of a pore, hence, the cutline passing through a tight junction followed by a pore was excluded from the graphical representations.

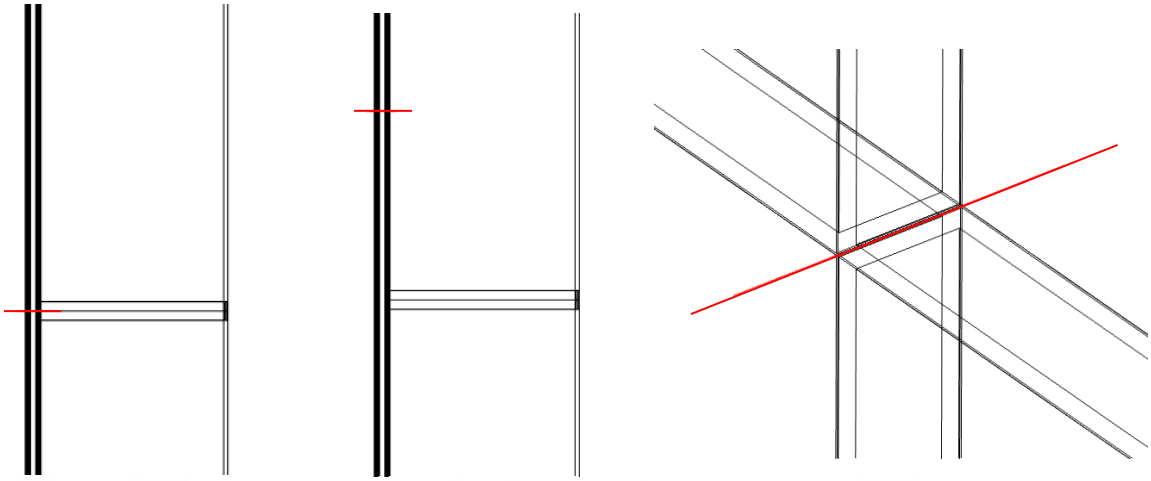

Figure 2.8. Representative image of the three main cutlines used in multilayer configuration after the introduction of the cell layer. a) cutline is passing through a cell located in front of a pore, b) cutline is passing through a cell located in front of polycarbonate and c) cutline is passing through a tight junction at the intersect of four cells in front of polycarbonate

3 RESULTS & DISCUSSION

3.1 Finite Element Analysis

The finite element method (FEM) introduced by Clough (1960), treats a continuous domain by smaller, discrete and finite domains. The solutions of the studied physics in the entire structure is represented by the collection of the solutions obtained from the finite elements. By the fast development of computer science, wide range of numerical solutions of differential equations has been adapted to finite element method and made available to commercial software engines.

The core of FEM lies on the process of meshing in which the geometrical domain is divided into smaller elements where the numerical solutions can be obtained easier to recreate the physical behavior of the studied model. The size of the mesh elements can range from very large (extremely coarse) to very small (extremely fine). If the coarse mesh is used, the accuracy of the results may be compromised depending on the study model. On the other hand, fine mesh size can produce large accuracy at the expense of larger processing memory and simulation time.

To the best of our knowledge, there has been no FEM-based study carried out to investigate the effects of the electric field on a fully constructed BBB-on-a-chip design with physiologically relevant elements such as the endothelial cell layer and the tight junctions.

3.2 Optimization of the Single-Layer Chip Configuration Effect of The Size and Distance of Electrodes

To optimize the best conditions for the fabrication of the chip and the manipulation of the endothelial barrier, several parameters were tested. Firstly, the effect of the size of the electrodes has been investigated by using electrodes with three different diameter values while keeping the center position of the electrodes the same. As can be seen in Fig. 3.1, the electric field and the current density significantly increased when the diameter was increased, which was expected due to the decrease in distance between two electrode edges.

(a)

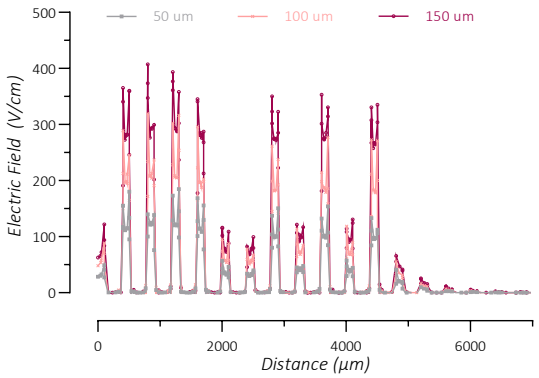

(b)

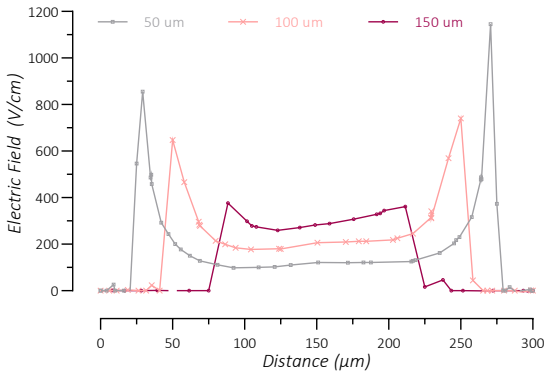

(c)

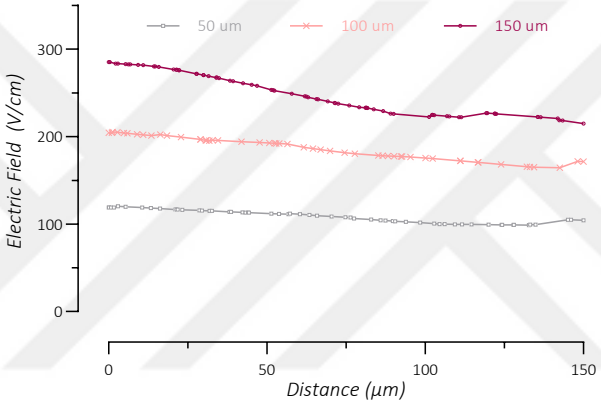

Figure 3.1 Effects of the electrode size on the electric field distribution (a) along the long axis of the channel (b) between the centers of two electrodes (c) along the height of the channel

The distribution of the electric field along the long axis of the BBB channel (Fig. 3.1a) showed that the electric field peaks on the corners of the PDMS pillars and decreases sharply in the gap between pillars, where the endothelial cells are expected to form a barrier. The difference of electric field between the corners and the gap was the highest for the largest diameter of electrodes. This should be kept in mind during experimentation as the endothelial cells located on the corners of the PDMS can be affected by the electric field significantly more than the endothelial cells in the gap. Next, the electric field between the centers of two electrodes was assessed (a total distance of 300 µm). As shown in Fig. 3.1b, the electric field peaks at the edges of electrodes and shows a homogenous distribution in the gap between two electrodes. The higher current density on the electrodes edges is due to the skin effect, in which the AC has the tendency of being concentrated near the surface of the conductor, for being reduced exponentially with greater depths in the conductor. It should be noted that the skin effect was

significantly lower for the 150 µm diameter electrodes, even though the value of the electric field in the gap was higher compared to smaller electrodes. This gives an advantage for larger electrodes for the experimental procedure as the highly concentrated electric field can damage the cells on top of and/or around the electrodes, especially in the brain chamber. Having a larger surface area, 150 µm electrodes distribute the electric field relatively better and prevent such a localization of high current for a given voltage and frequency.

Considering the endothelial cells are expected to be stacked on top of each other in the gap between two pillars and placed on the middle of the two electrodes, it is crucial to look at how the electric field changes within the height of the channel at this position. As the electrodes are thin film deposited and represent the 2D constructs of the system at the bottom of the structure, it was expected for the electric field to decrease along the Z-axis. All three different sizes of electrodes had a certain decrease in the electric field from the bottom towards the top of the channel (Fig. 3.1c), with the largest decrease found to be for 150 µm diameter electrodes. It can be explained as the distance between the electrodes decreases (larger diameter), the current cannot reach to further distances from the electrodes. But it should be noted that the value of the electric field, even at the very top of the channel, was significantly higher compared to smaller electrodes.

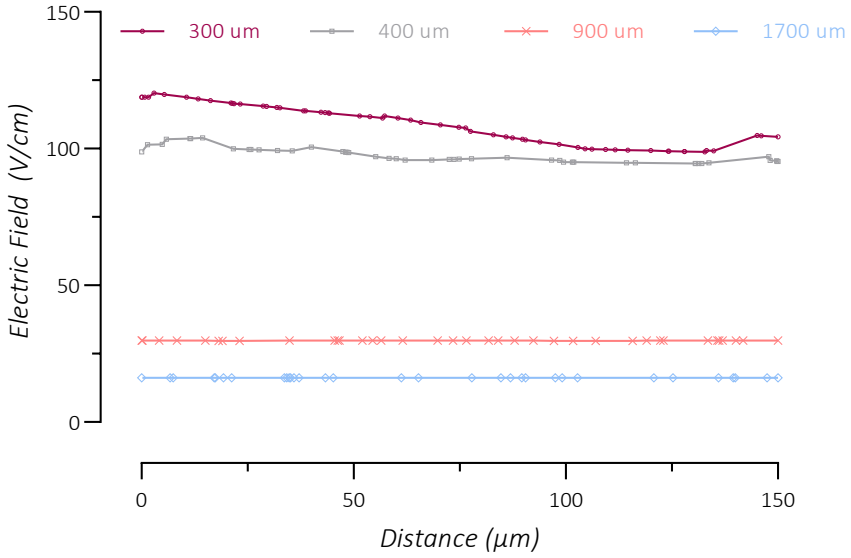

Figure 3.2. Effect of the distance between electrodes on the electric field distribution along the height of the channel

To better understand the decrease of electric field in the Z-axis, the smallest electrodes (50 μm) were placed at different distances. As the distance between the center of electrodes increases from 300 μm to 1700 μm, the distribution of the electric field became more homogenous (Fig. 3.2). Even though the decrease of electric field in the Z-axis for the electrodes that are placed 300 μm away was larger compared to more distant situations, this decrease is compensated by the significantly higher value of electric field. In order to have a reasonable electric field over the vertical stack of endothelial cells, this result shows the importance of putting the electrodes as close as possible to each other. Moreover, it is important to put electrodes close to the endothelial cell barrier in order to reduce the field over astrocytes and pericytes in the brain chamber, which also requires the electrodes to be as close as possible to each other.

In the interest of having the theoretically calculated voltage-to-distance electric field values; a more homogenous distribution between the electrodes and lower skin effect; and last but not least, an easier integration during the fabrication process, 150 μm diameter electrodes have been chosen to proceed with in the following simulation/experiments.

3.2.2 Effects of the Electrode Paths

Even though using the circular electrodes on the COMSOL Multiphysics® simulation gives enough information about the electric field distribution over the structure, it is important to assess the effect of the electrode paths as they will be passing through the entire brain chamber and may result in unwanted effects. For this reason, paths with 70 μm width were introduced to electrodes both in the endothelial channel and the brain chamber, similar to the real design of the chips. As shown in Fig. 3.3, there were no significant effects of the presence of paths on neither the distribution nor the values of the electric field. Similar to the simulation without paths, the electric field in the brain chamber was still less than 10 V/cm, suggesting the presence of paths had no particular effect on the electric field distribution in the brain chamber either (data not shown).

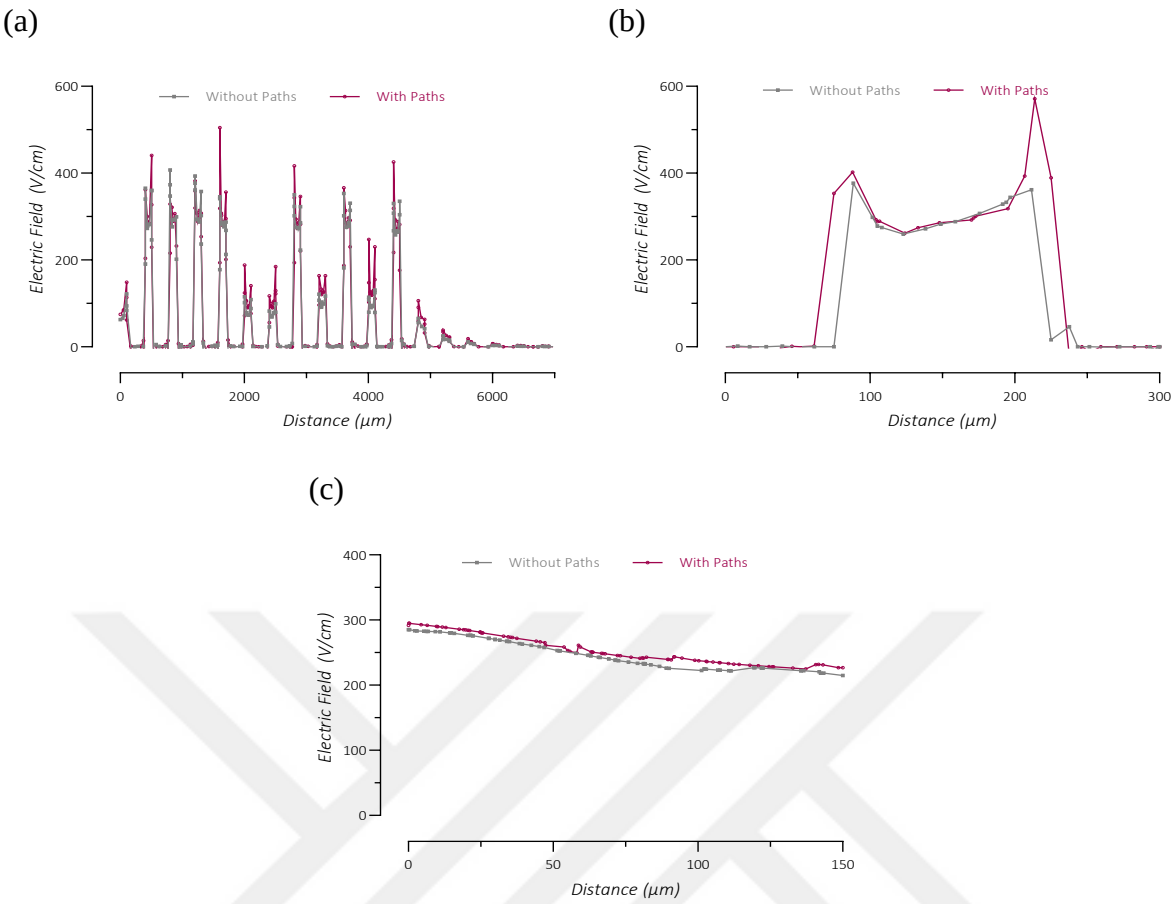

Figure 3.3. Effects of the electrode paths on the electric field distribution (a) along the long axis of the channel (b) between the centers of two electrodes (c) along the height of the channel

3.2.3 Replacing Top Electrodes with a Single Rectangular Electrode

To reduce the interaction of the electrode paths with the astrocytes and pericytes and the possible passivation of the electrodes, it is desirable to reduce the number of electrode paths in the structure. For this reason, a different structure has been designed by replacing all top electrodes with a single rectangular electrode. When compared to the previous design, it has been found that the electric field was overall higher when all the electrodes are individual and circular (Fig. 3.4). Not only this, but also putting a single rectangular electrode that spans from the left end of the of the channel to the point where the last circular bottom electrode is located resulted in an increase of the electric field at undesired locations, for instance in the gaps where no circular electrodes were present. The idea of using individual electrodes is to be able to manipulate individual endothelial barriers located in each gap. Even though it makes the fabrication relatively easier and reduces the possibility of leaks, using a single rectangular electrode may change the permeability of the off-target endothelial barriers, compromising the promise of individual manipulation. Also, the presence of PDMS pillars prevents the

rectangular electrode to come closer to the bottom electrodes, which increases the distance between them and hence reduces the electric field in the gap where endothelial cells are expected to form the barrier.

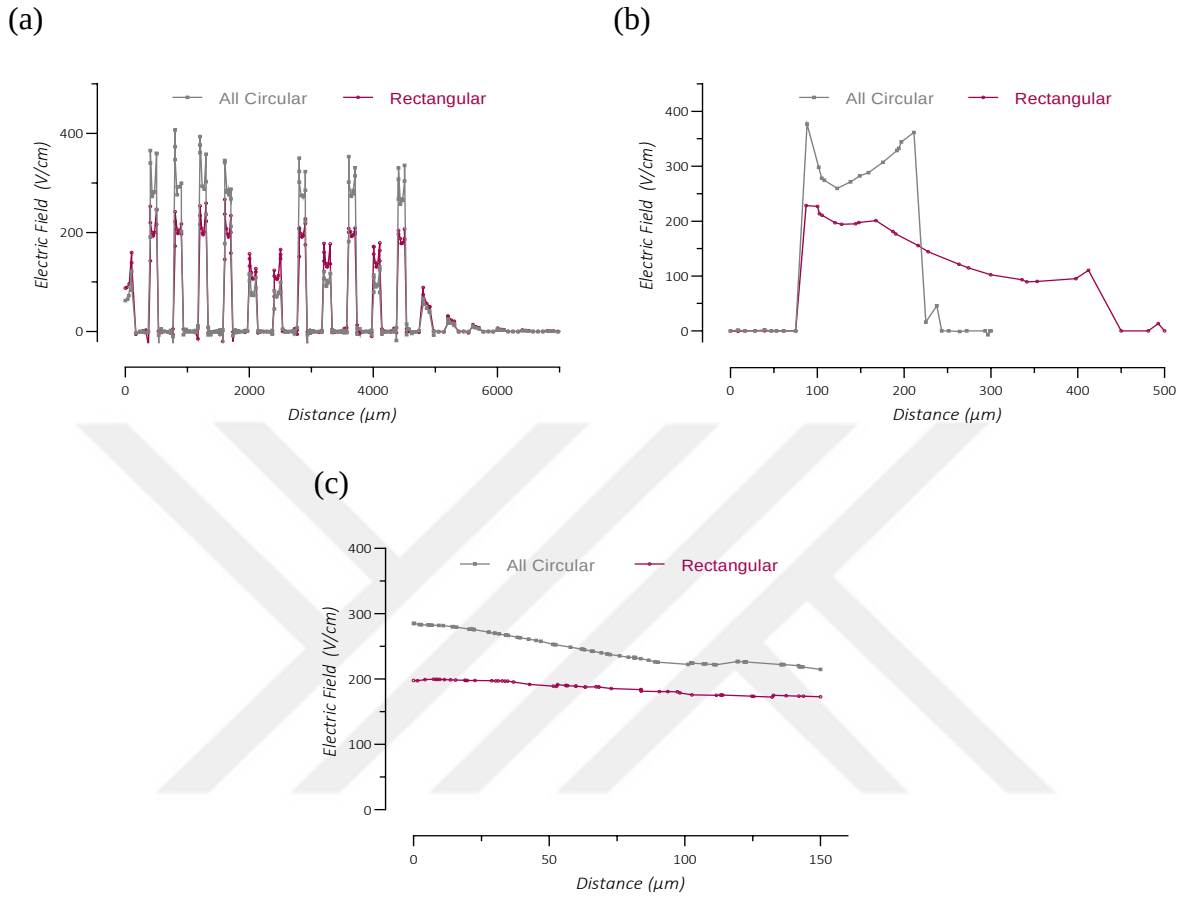

Figure 3.4. Effects of the electrode shape on the electric field distribution (a) along the long axis of the channel (b) between the centers of two electrodes (c) along the height of the channel

3.3 Introducing the Cell Barrier in the Single-Layer Configuration

The most crucial part of the experiment is to understand the differences of electric field and current distribution over the cell structure and the gaps between cells, i.e. the tight junctions, which in turn will determine if the outcome permeabilization is achieved through a transcellular or paracellular pathway. To understand the differences between these two regions, a cutline extending between 0.5 μm before and after the cell is compared to another cutline with the same length that is passing through the tight junction. After the introduction of two cell structures with a highly resistive cellular membrane ($\sigma_m=10^{-7}$ S/m), the potential distribution over the structure changed significantly. Due to the presence of a highly resistive element (cell) in the structure, the potential drop over the channels were reduced compared to the control (without cells) model and a significant potential drop is found over the cellular layer, namely over the

front and back membrane of the barrier with almost no potential change over the cytoplasm (Fig. 3.5).

a)

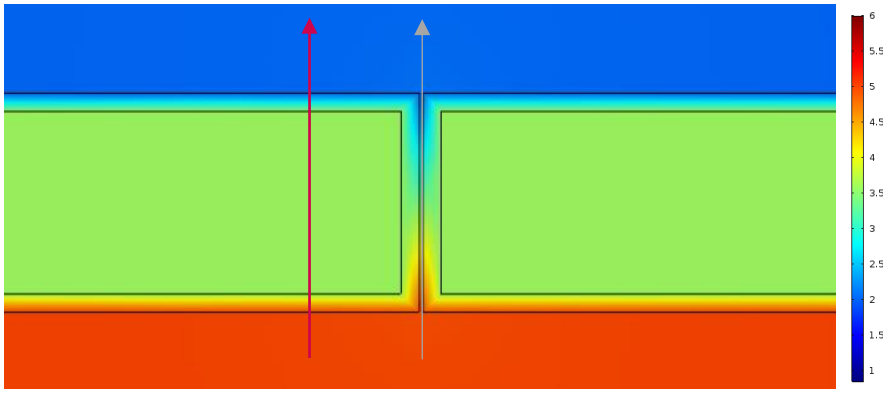

b)

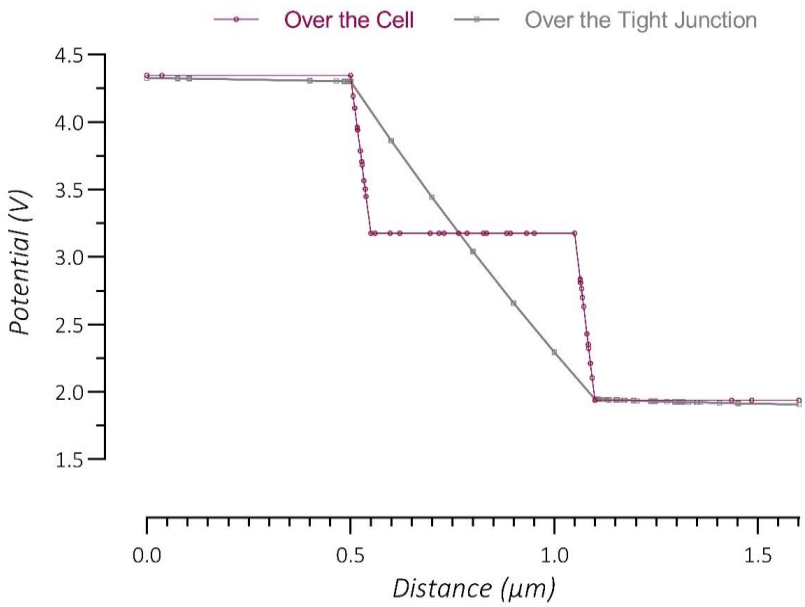

Figure 3.5. Potential distribution over the cell layer in the single layer configuration a) color image of potential distribution from top view and b) along the cutline passing either i) through the cell structure or ii) through the tight junction

To understand the behavior of the cell in the single-layer structure, an equivalent electrical circuit can be designed. Given the parameters in Section 2.1, the cell layer can be represented by both resistance and capacitance characteristics. Resistance characteristics of the cell layers come from the intrinsic resistivity of the lipid bilayer against the current flow. Due to the accumulation of the charges at two sides of the lipid bilayer, where the conductive extracellular fluid (PBS) and the intracellular fluid (cytoplasm) acts like a parallel plates, the cell membrane

also shows characteristics of a capacitor, defined by the dielectric constant of the cell membrane, the total surface area and the thickness of the cell membrane. On the other hand, the conductive parts of the chip, namely the channels, cytoplasm and the tight junctions could be represented by a simple resistance defined by the conductivity of the solution, length of the solution and the surface area according to Ohm's law. Especially at low frequencies, the double layer capacitance of the electrodes should also be considered.

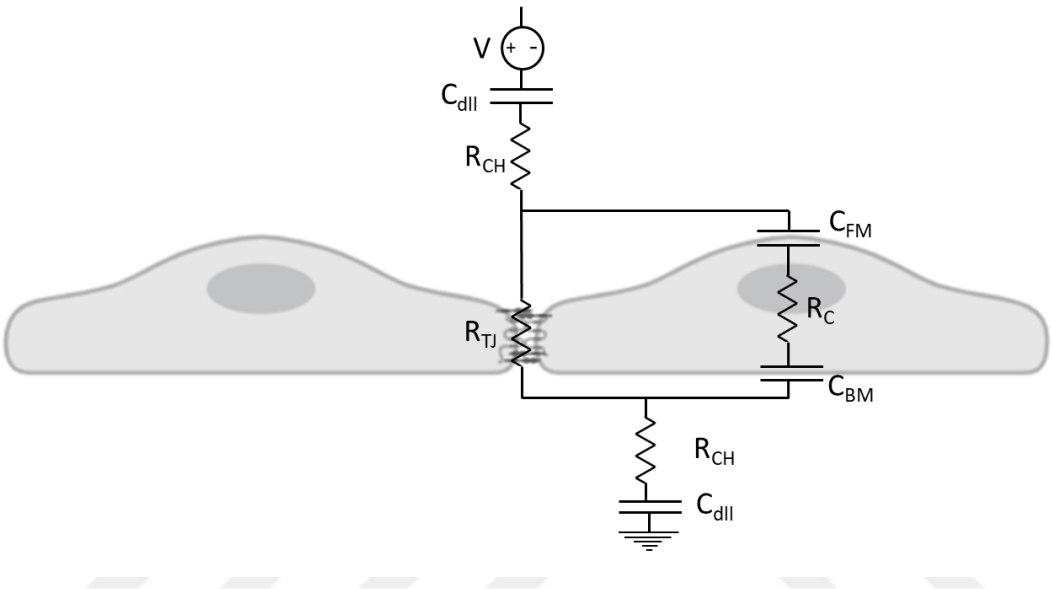

Figure 3.6. Simplified equivalent circuit model of the cell layer between two PDMS pillars. Top part represents the BBB channel and the bottom part represents the brain chamber. Resistance of the channels, the tight junctions and the cytoplasm is given as R_{CH}, R_{TJ} and R_C, respectively. Double layer capacitance of the electrodes and the capacitance of the front and back membrane are given as C_{dll}, C_{FM} and C_{BM}, respectively.

The complete equivalent circuit can further be simplified into Fig. 3.6. As the resistance of the cell membrane is significantly larger than the capacitance of the cell membrane, which are connected in parallel in the circuit model, the current would mostly go through the resistive element. Hence, the cell layer can be represented by two cell membrane capacitances and one cytoplasm resistance connected in series.

Keeping this model in mind, the current is not expected to flow through the cell layer because of the high capacitance of the cell membrane at low frequency. As the membrane has low conductivity, the charges accumulated in the two sides generate a similar relatively large potential drop over the front and back membrane of the cell layer. As connected in parallel, the total potential-drop over the tight junction acquires a similar total potential drop as of the cell

layer. However, with a much smaller slope of the potential drop compared to the front and back membrane.

As the consequence of the potential drop, two electric field peaks were found for the front and the back membrane of the cellular structure (Fig. 3.7). These peaks reached extreme values, up to ~250,000 V/cm, compared to ~100-200 V/cm electric field in the rest of the structure. Corresponding to the linear decrease of potential, the electric field was relatively higher (~50,000 V/cm) in the tight junction compared to the endothelial channel and the brain chamber but significantly smaller compared to the front and back membrane. Inside the cytoplasm, due to the nearly constant potential, the electric field was found to be almost zero. This result shows the significance of this simulation-based model, in a sense that even the voltage-to-distance ratio is kept as 300 V/cm, the electric field on the cell layer will be approximately a thousand times more than this value. This suggests that the studies conducted *in vitro* to understand the thresholds of reversible and irreversible electroporation, and hence the range of electric field that leads to paracellular or transcellular permeabilization, underestimate the real electric field value that exists on the cell.

While the voltage-to-distance ratio of electric field depends only on the applied voltage and the distance between two electrodes, the real electric field that the cells are exposed to depends on many other factors, such as the total surface area, the thickness, resistivity and the dielectric constant of the cell layer and the distance between the cells that current can flow through, i.e., the side of the tight junctions. All these factors determine the amount of charges collected at the two sides of cell layer, which in turn determines the potential drop and hence the electric field over the cell layer. The strength of this electric field determines not only the size of the induced pores but also the recovery of the cell membrane. Together, this finding suggests that investigation of the real electric field values on the cell membrane can be an important tool to understand the range of paracellular/transcellular permeabilization and the thresholds of reversible/irreversible electroporation that leads to a better ability of tuning the characteristics of the BBB-on-a-chip *in vitro*.

a)

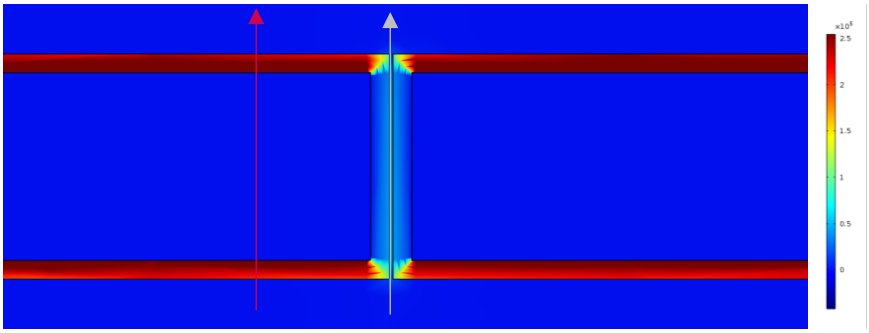

b)

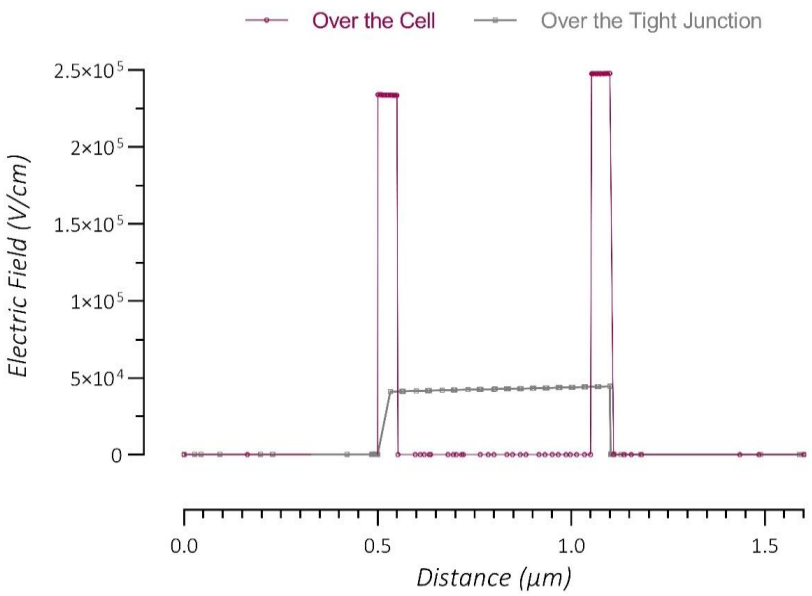

Figure 3.7. Electric field distribution over the cell layer in the single-layer configuration a) color image of electric field from top view and b) along the cutline passing either i) through the cell structure or ii) through the tight junction

Unlike the electric field, the current density cannot have large values inside the cell structure due to the high resistivity of the cellular membrane against the current coming from the channel. The current density analysis across the cell and the tight junction showed that the current is almost completely localized in the tight junction and retains extremely low values inside the cell. This suggests that current, at least in given frequency of 1 Hz, can only pass through the gap between the cells, but not through them. In the scaled inset of Fig. 3.8b, the current density can be seen to decrease down to zero in the cell while it increases up to ~700 A/cm^2 in the tight junction. In the rest of the endothelial channel and the brain chamber, the current density retains low values around 2-4 A/cm^2 which can be understood as the total current is distributed to the large cross-sectional area of the channels.

a)

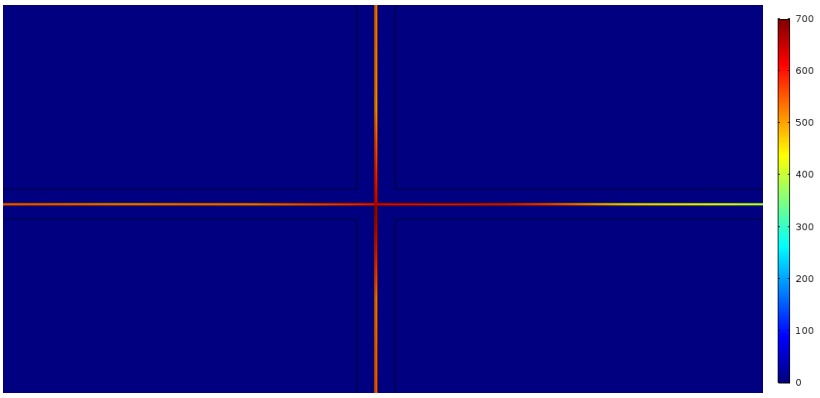

b)

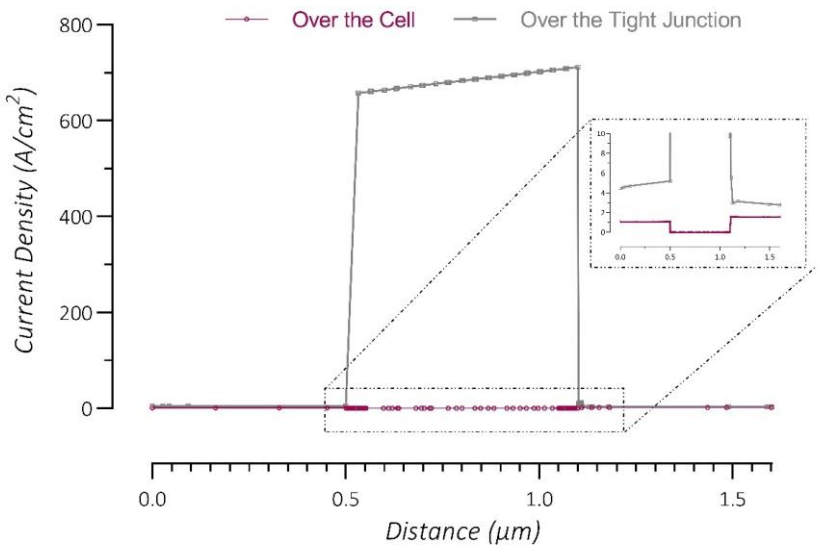

Figure 3.8. Current density distribution over the cell layer in the single-layer configuration a) color image of current density from the front view, showing the tight junctions at the intersect of four cells and b) along the cutline passing either i) through the cell structure or ii) through the tight junction

This result shows that at extreme low frequencies, the amount of current passing through the unit area of the cell will be significantly lower than the amount of current passing through the unit area of the tight junction. However, as explained in Section 1.5, it has been shown that even at these low frequencies (i.e. 1 or 200 Hz), it is possible to obtain both reversible and irreversible electroporation. To understand this effect, it is required to obtain the correct current density value over the cell that leads to either paracellular/transcellular or reversible/irreversible electroporation and the correlation between the current density obtained and the parameters used in the study such as the amplitude and frequency of the electric field and the duration and

number of the pulses. To the best of our knowledge, no such study is carried out. As the experimental calculation of parameters such as the electric field and the current density over the cell layer is not straightforward, it is recommended to carry out the corresponding simulation for each different set of parameters used during the experiment in order to make a complete correlation between the electric field and/or current density over the cell layer and the observed effects on permeabilization.

Lastly, the distribution of the electric field and the current density was plotted along the height of the chip (Fig. 3.9). Accordingly, one cutline was taken along the front membrane of the cell layer and the other was taken in the middle tight junction, both extending from the bottom of the chip to the top of the chip. The results revealed that neither the electric field nor the current density changes significantly between the cells located at the bottom of the chip and the cells located at the top of the chip. Considering the electric field at the top of the chip was reduced almost one-third of its value at the bottom of the chip in the control group (Fig. 3.1c), the addition of the cell layer can be said to result in a more homogenous distribution of the electric field by localizing the majority of electric field in the cell memrane and the majority of the current density in the tight junctions and hence, minimizes the differences with respect to cell position otherwise expected previously.

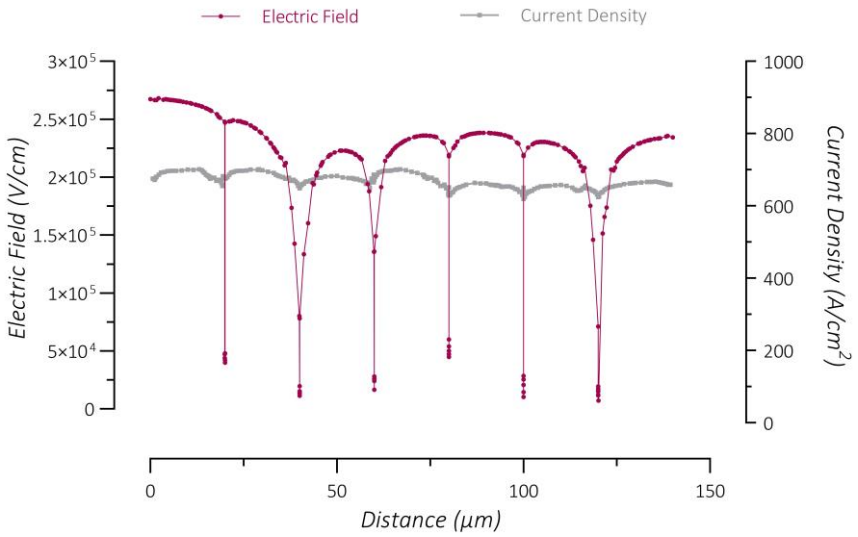

Figure 3.9. Electric field and current density distribution inside the cell membrane and the tight junctions, respectively, along the height of the chip

3.4 Distribution of Potential, Electric Field and Current Density in the Multilayer Chip Configuration

The major difference between the single-layer structure and the multi-layer chip lies on the use of highly resistive porous membrane separating the two chambers. The finite element analysis showed that the presence of such a non-conductive polycarbonate layer in the multilayer configuration significantly alters the distributions of three main electrical parameters assessed in this study. The color image in Fig. 3.10 shows the decrease of potential is almost completely localized over the polycarbonate membrane in the middle of the structure while there is barely any change of potential in the rest of the structure. This can be understood by the fact that the polycarbonate membrane has 14 power of magnitude times higher resistivity and a significantly smaller dielectric constant compared to the surrounding PBS if these two elements are considered as two current paths connected in series.

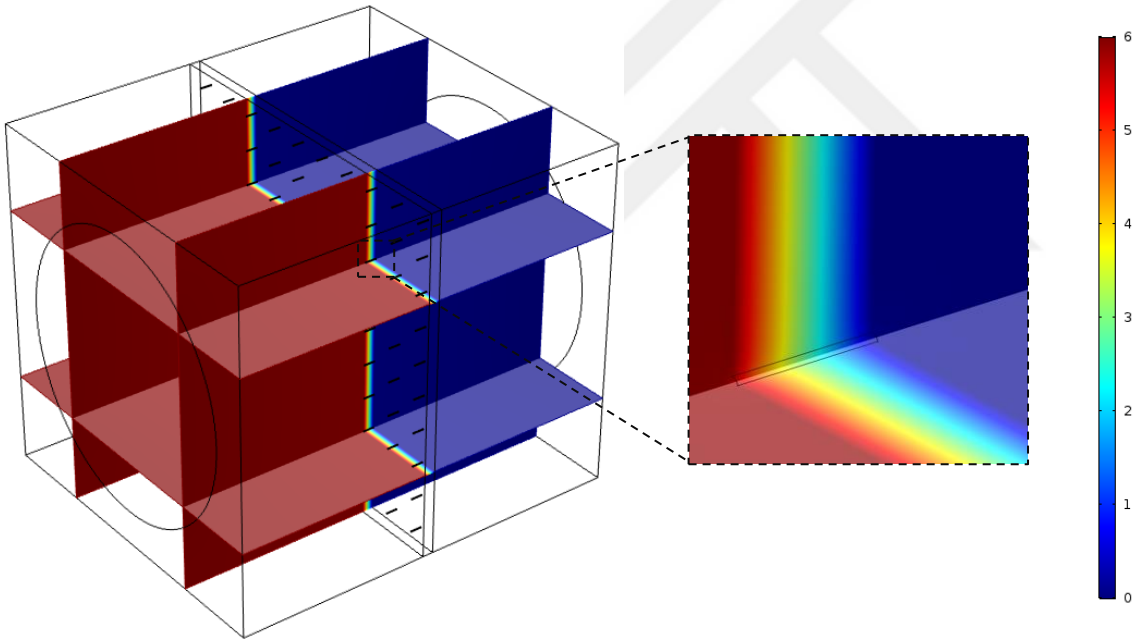

Figure 3.10. Color image of the potential distribution inside the multilayer chip with the scaled image of a pore inside the polycarbonate membrane.

The presence of pores distributed over the polycarbonate membrane suggests that these two parts of the structure might have different properties and eventually different impacts on the cell layer that will be in front of them. Therefore, the potential decrease over a cutline passing through the polycarbonate has been compared to another cutline passing through one of the pores at the middle of the membrane. According to Fig. 3.11, the potential almost entirely decreases over the porous membrane, regardless of passing polycarbonate or a pore. This

suggests that the polycarbonate region and the pores act like two current paths connected in parallel, with an almost same potential drop over them. Significantly smaller decrease of potential can be observed inside the endothelial and brain channels in scaled part of the graph at left. Another important observation can be seen towards the end of the endothelial channel; the decrease of potential starts relatively earlier in front of the pores due to the continuity between the channel and the pore. On the other hand, the potential starts decreasing only at the starts of the polycarbonate region but not beforehand due to the discontinuity of the channel and the polycarbonate and the large difference of the electrical properties of these two structural elements. This is yet another significant finding of the simulation and suggests that the potential drop in the close proximity of pores will be larger than the potential drop in front of the polycarbonate.

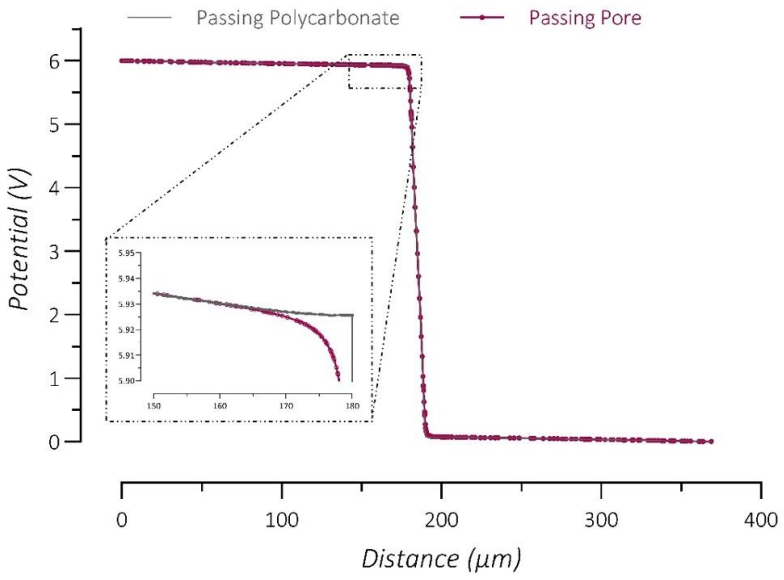

Figure 3.11. Potential distribution along the cutline between two electrodes passing either i) through the polycarbonate or ii) through one of the pores inside the membrane

To confirm the expected consequences of the potential distribution, the electric field inside the entire structure is measured. Corresponding to the sharp potential decrease over the porous membrane, the electric field is found to increase to large values in the porous membrane while it retains low values in the endothelial channel and the brain chamber. The scaled color image on the right (Fig. 3.12) also shows how the electric field starts increasing earlier in close proximity of the pore but not in front of the polycarbonate region of the porous material.

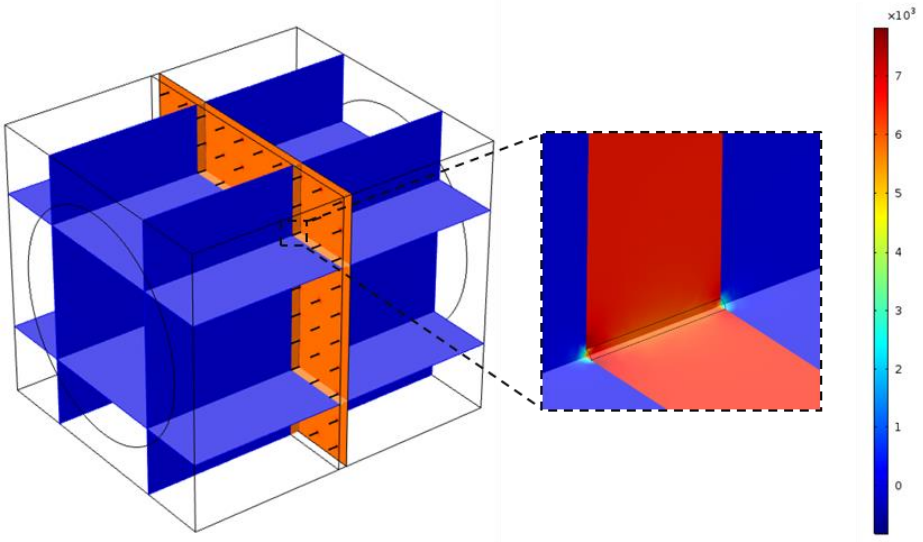

Figure 3.12. Color image of the electric field distribution inside the multilayer chip with the scaled image of a pore inside the polycarbonate membrane.

Like the potential distribution, two different cutlines were taken to graphically represent the difference between the electric field distribution over the polycarbonate and one of the pores. As shown in Fig. 3.13, electric field reaches large values over the porous membrane, both in the polycarbonate region and the pore. Similarly, the left inset in Fig.3.13 shows that the electric field starts changing earlier (approximately 2 μm before the pore) and increases gradually to its highest value in front of the pore, while no such gradual increase is seen for the case of polycarbonate, where the electric field sharply peaks only when it encounters the polycarbonate.

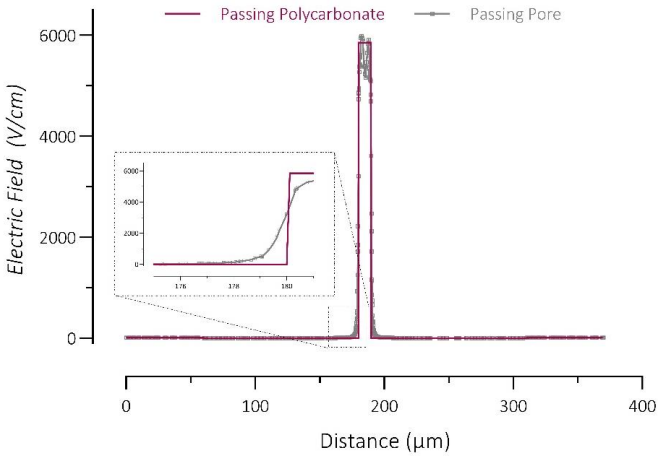

Figure 3.13. Electric field distribution along the cutline between two electrodes; passing either i) through the polycarbonate region of the membrane or ii) through one of the pores inside the membrane

Not only to see the difference between the polycarbonate and the pores better, but also to see the difference between the corners of the porous membrane and its central region, a diagonal cutline is taken, extending from the bottom corner of the porous membrane to the opposite top corner as depicted in Fig. 3.14. To see the electric field distribution in the region where endothelial cells are expected to grow, one diagonal cutline is taken at the middle of the porous material (x=185) while the second diagonal cutline is taken 1 μm in front of the porous membrane. As evident in Fig. 14b, when the diagonal cutline is passing in the middle of the porous membrane, there is a decrease of electric field each time it passes through a pore, approximately from 6000 V/cm to 5000 V/c. This corresponds to a slight difference between the potential drop over the polycarbonate and the pore. On the other hand, when the diagonal cutline is located 1 μm before the porous membrane, there is an increase in the electric field each time it passes in front of a pore, while its value remains close to zero in front of polycarbonate regions. This is the direct consequence of the fact that the potential starts to decrease earlier in front of a pore and remains almost constant in front of polycarbonate (left insets in Fig. 3.11 and Fig. 3.13).

And lastly, the diagonal cutline analysis revealed no significant difference of electric field distribution between the corners and the center of the porous membrane (Fig. 3.14). This can be understood as the diameter of the electrodes are almost the same size with the porous membrane and they are positioned in parallel to the porous membrane, which creates a symmetric distribution of electric field over the entire surface of the porous membrane. This can be considered as an important difference between the single-layer and the multi-layer chip configuration. As shown in Fig. 3.1c, the electric field and the current density was not distributed homogenously in the single-layer configuration, but rather both of these parameters were found to decrease along the height of the chip, given that the electrodes are located at the bottom of the chip. Even though the distribution of these parameters were found to be not significantly different between the bottom and the top of the chip once the cell layer is introduced in the single-layer design, it should be kept in mind during the experimentation that the multi-layer configuration gives the most homogenous distribution of electric field and the current density over any chosen cross sectional area of except for the porous membrane.

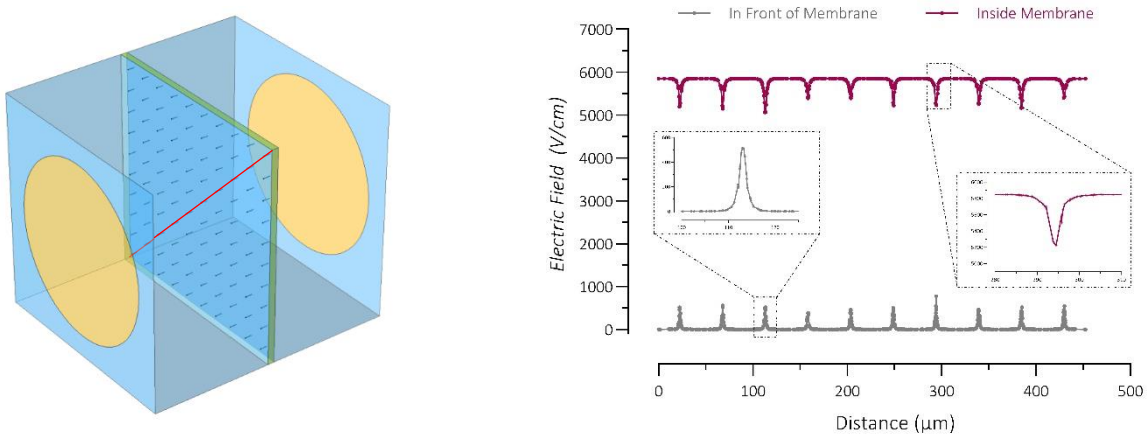

Figure 3.14. Electric field distribution along the diagonal cutline between two opposite corners of the porous membrane passing either i) in front of the membrane (x=179) or ii) at the middle of the membrane (x=185)

Even though the electric field distribution can be directly related to the potential distribution over a given structure, the current created by the applied voltage may not follow the same distribution when the insulators are included in the system. Considering the current is one of the most important factors on the disruption of the cellular structures, it is important to see how the current is distributed in the chip. Color images of current density distribution shows that the current is almost zero inside the polycarbonate but instead localizes inside the pores (Fig. 3.15). Streamline analysis also support this finding; the current lines change their trajectories as they approach to porous membrane and enter the closest pore (data not shown).

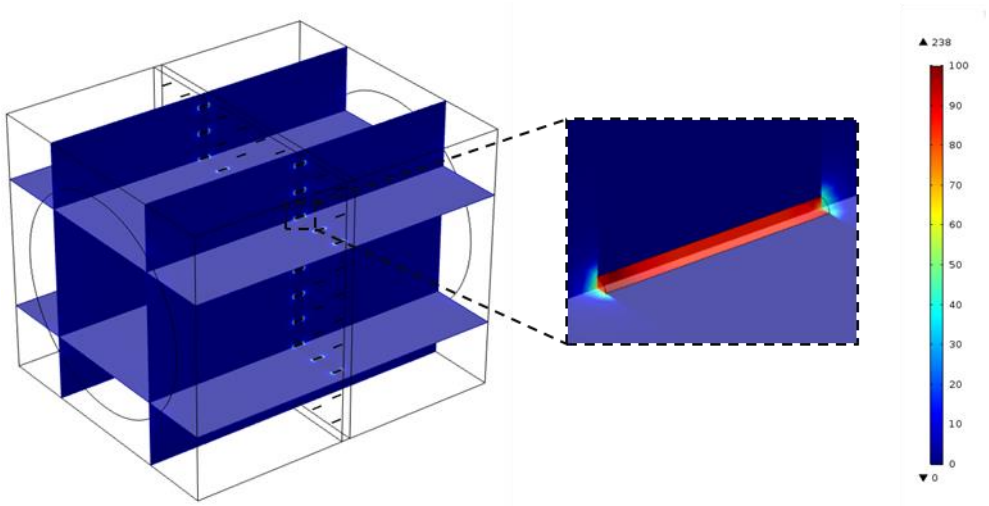

Figure 3.15. Color image of the current density distribution inside the multilayer chip with the scaled image of a pore inside the polycarbonate membrane.

Like the potential and electric field distribution, one cutline passing through the polycarbonate region of the porous membrane is compared to another cutline passing through one of the pores. Unlike the previous two cases, the current density shows a significant difference between these two regions of the porous membrane. As can be seen in Fig. 3.16, the current density increases up to 100 A/cm^2 inside the pores, which reflects its concentration inside these small *tunnels*. On the other hand, the current density sharply drops to zero when the cutline is passing through the polycarbonate. This result was expected as the polycarbonate has almost no conductivity compared to the pores and current cannot flow through it in low frequencies. In the rest of the structure, namely in the endothelial channel and the brain channel, the current density remains at significantly lower values between 0.06-0.08 A/cm^2 due to the large cross-sectional area that the total current distributes in.

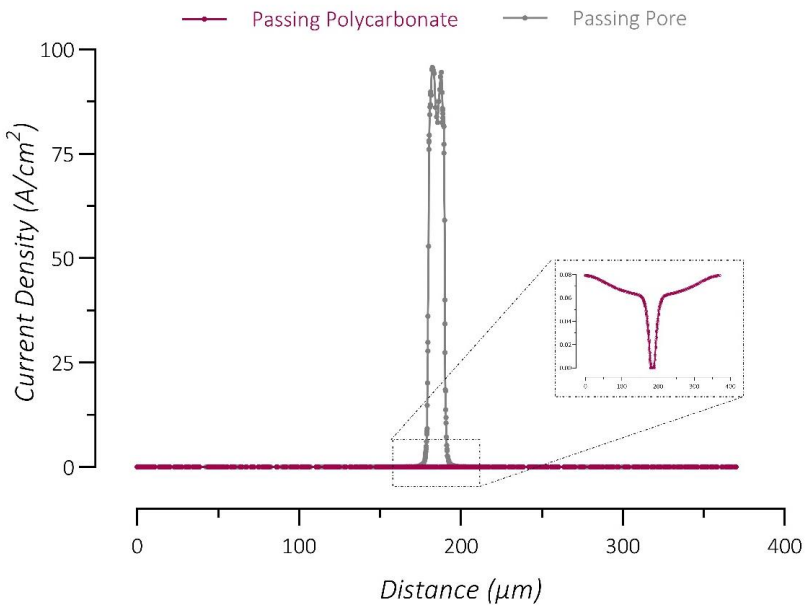

Figure 3.16. Current density distribution along the cutline between two electrodes; passing either i) through the polycarbonate region of the membrane or ii) through one of the pores inside membrane

The diagonal cutline analysis confirmed that the current peaks inside the pores and remains zero in the rest of the porous membrane (Fig. 3.17). When the diagonal cutline is positioned just in front of the membrane, relatively smaller peaks of current density can be seen in front of each pore. This indicates that at a given distance of approximately 1-2 μm from the membrane, the current density already starts localizing, however, stays less concentrated compared to the pores. Like what is observed in the electric field, no significant difference of current density is found between the corners and the center of the porous material.

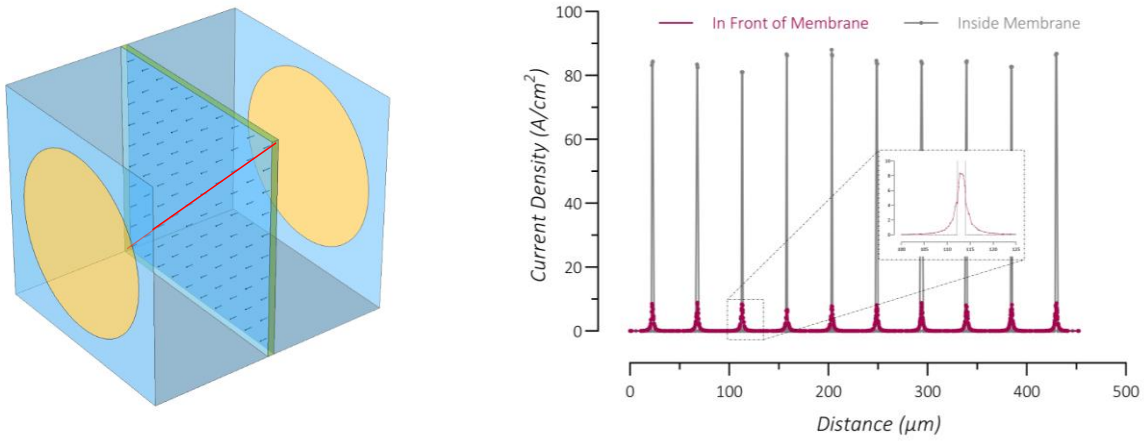

Figure 3.17. Current density distribution along the diagonal cutline between two opposite corners of the porous membrane passing either i) in front of the membrane (x=179) or ii) at the middle of the membrane (x=185)

3.5 Introducing the Cell Barrier in the Multilayer Configuration

In order to have an approximately same cross-sectional area of the cell layer in the single-layer configuration for the comparison purposes, a cell layer composing of 9 cells with 50 μm x 20 μm x 0.5 μm dimensions are introduced 10 nm in front of the porous membrane. To avoid the meshing problems and make it easier to simulate, the width of the cellular membrane was increased to 50 nm from its physiologically relevant value of 5-10 nm, same as in the single-layer model.

As explained in the previous section, the main difference of the multilayer configuration from the lateral chip is the presence of a porous membrane with an extremely small conductivity. Therefore, it is important to investigate the effects of the polycarbonate and pore regions of the porous membrane on the cell layer individually and to compare the results to the tight junctions located in front of the polycarbonate. Compared to other scenarios, having a tight junction directly in front of a pore has a very low probability due to the low porosity of the membrane, hence the effect of a pore on a tight junction is excluded from the analysis. Overall, three different cutlines extending 0.5 μm before and after the cell layer passing either i) a cell in front of the polycarbonate, ii) a cell in front of a pore and iii) a tight junction in front of the polycarbonate were graphically analyzed.

Fig. 3.18a shows the largest potential decrease occurs over the back membrane of the cell in front of the pore, followed by the back membrane in front of the polycarbonate, the front membrane regardless of the location and finally the tight junction in front of the polycarbonate.

It can also be seen that at the presence of a cell layer in the system, the potential decrease over the porous membrane significantly changes. This can be understood as the addition of another high resistive element to the system results in a redistribution of the potential that was previously confined almost entirely over the porous membrane. But the most relevant information that we can extract from these results is the clear different behavior of the total potential decrease in the front and back cell membrane.

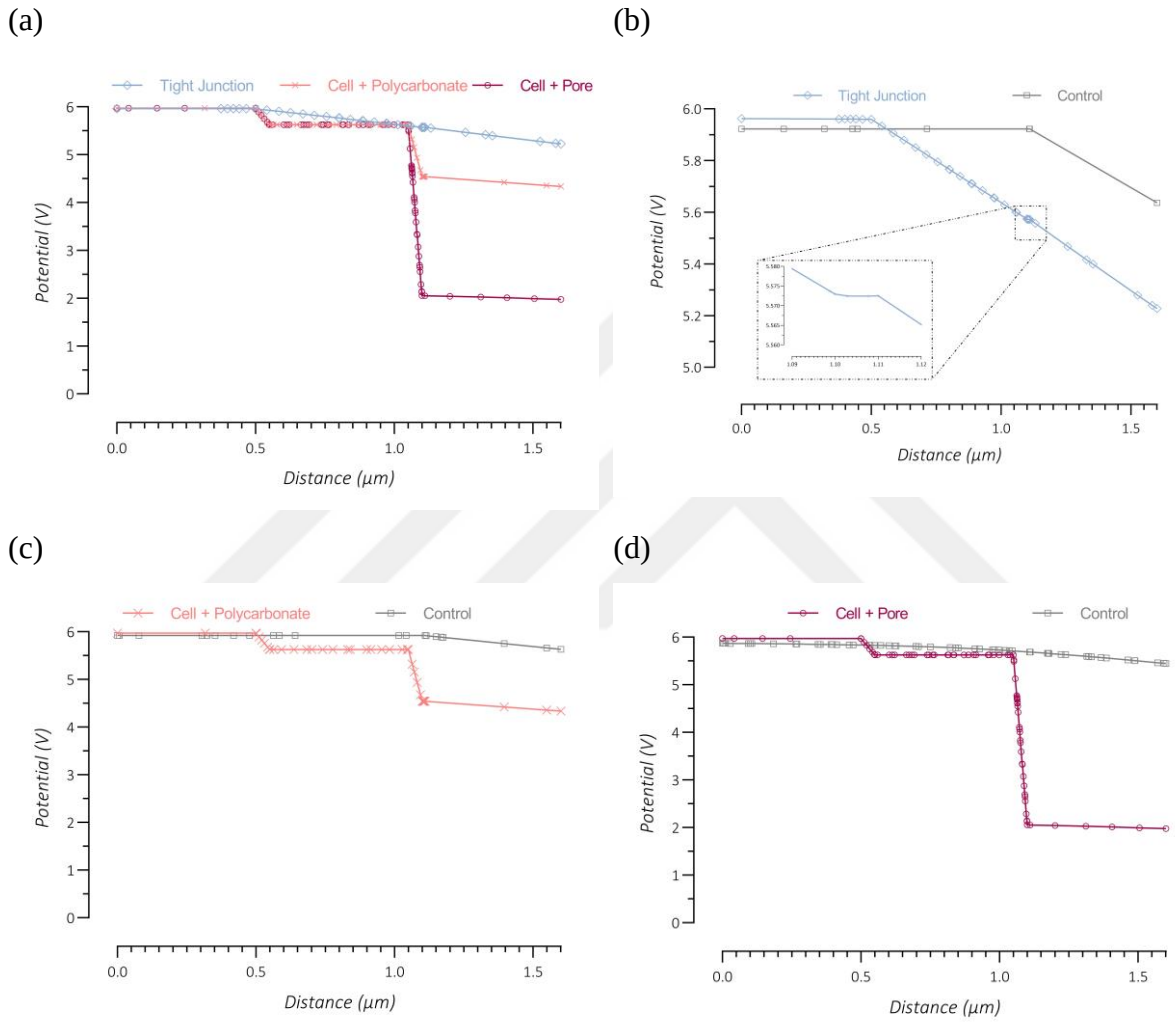

Figure 3.18. Potential distribution over the cell layer in the multilayer configuration along the cutline passing either i) through a tight junction positioned in front of the polycarbonate, ii) through a cell positioned in front of the polycarbonate or iii) through a cell positioned in front of a pore

To understand and discuss the individual elements in the system, it might be helpful to consider the circuit equivalent of the multilayer chip design with the cell layer. According to cell dielectric properties, the cell layer once again can be represented by the capacitance of a cell membrane and the resistance of the cytoplasm. As the current can either flow through the cell

layer or through the tight junctions, the total impedance of the cell layer can be represented as connected in parallel with the resistance of the tight junctions. Like the single-layer chip, the BBB channel and the brain chamber can be approximated as two resistors with a certain resistivity, cross sectional area and length.

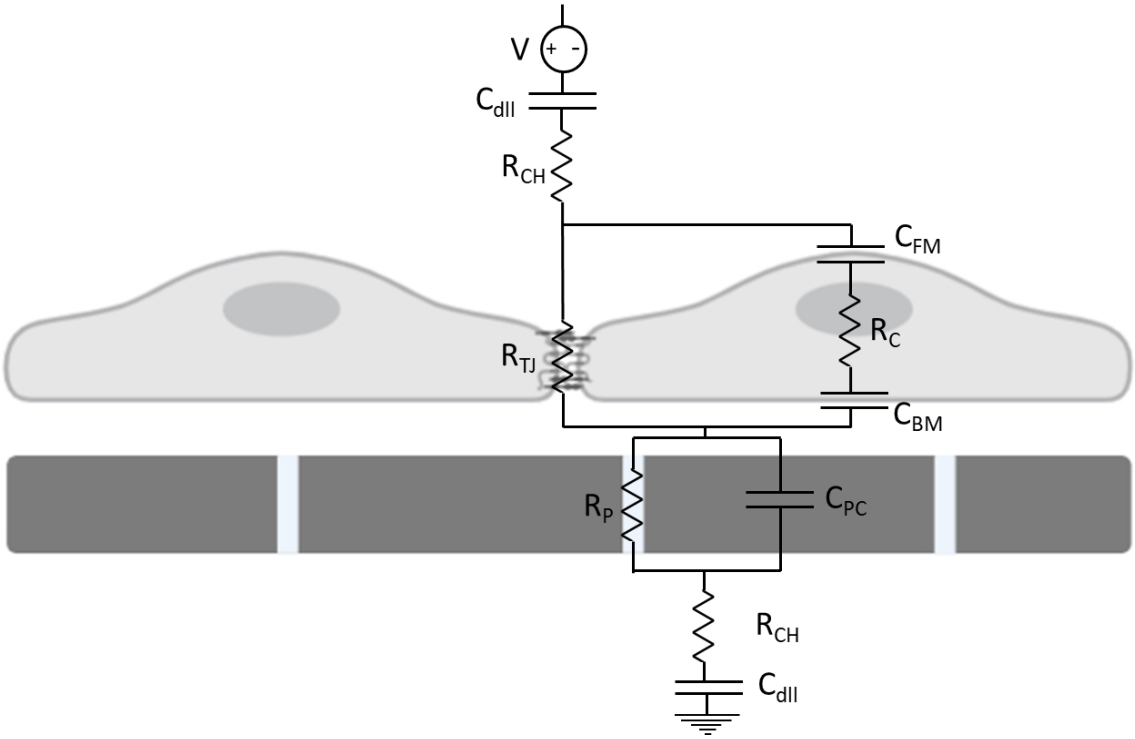

Figure 3.19. Simplified equivalent circuit model of the endothelial cells in front of the porous polycarbonate membrane. The cells are scaled up for the easier interpretation. Resistance of the channels, the tight junctions, the cytoplasm and the pores are given as R_{CH}, R_{TJ}, R_C and R_P, respectively. Double layer capacitance of the electrodes and the capacitance of the front membrane, back membrane and the polycarbonate membrane are given as C_{dll}, C_{FM}, C_{BM} and C_{PC}, respectively.

Specific to the multilayer chip, two more elements can be introduced in the circuit; the polycarbonate and the pores, which are connected in parallel to represent two possible paths for the current passing through the porous membrane. Like cellular membrane, polycarbonate also acquires a charge accumulation at two sides where the conductive channels are located, for this reason the polycarbonate part of the porous membrane can be represented by capacitance properties that are given by the dielectric constant, the thickness and the cross sectional area of

the polycarbonate, which is connected in parallel to the intrinsic resistance of the polycarbonate given by its resistivity. On the other hand, the pores in the system can be represented simply by their resistance value, similar to the tight junctions. This complete circuit can be further simplified by the removal of the resistance characteristics of the cell membrane and the polycarbonate as the current would not pass through these elements as explained before (Fig. 3.19).

To understand the behavior of individual structural elements, the results after the introduction of the cell layer is compared to the control (no cell layer) results. Comparing the potential decrease over the tight junction to the control group reveals that the potential sharply decreases over the tight junction even though it is intrinsically a conductive region. This potential decrease, however, was not the same with the potential decrease over the surrounding cell layer. This result was significantly different from the results of the single-layer chip where the cell layer and the tight junction behave like ideal electrical components connected in parallel and acquire a similar total potential drop over them. It can be clearly seen in Fig. 3.18 that in the multilayer configuration due to the presence of a highly resistive and charged membrane the potential drop over the cell layer, regardless of where it is located, is significantly larger than the total potential drop over the tight junction. This already suggests that the distribution of the electrical parameters is not homogenous over the cell barrier and the equivalent circuit may not be addressed to explain several of these findings.

For instance, comparing the potential decrease over the cell layer located in front of the polycarbonate to the control group revealed that the potential decrease was slightly larger in the back membrane compared to the front membrane. This was the direct consequence of the use of the polycarbonate membrane for the attachment and growth of the cells and highlighted a crucial difference between the single-layer and the multilayer structure. Once the cell layer was located at a close proximity to the porous membrane, the charges accumulated at two sides of the porous membrane (due to its capacitance properties) are constricted in a nanometer size distance (10 nm), which resulted in a large amount of charges accumulated outside of the back membrane. At this point, even the capacitance of the front and back membrane was completely the same, the potential drop over the back membrane was significantly larger (~3.5 V) compared to the potential drop over the front membrane (~0.5 V)

The similar result can be seen for the cell structure located in front of a pore, but with a much greater extent of potential decrease over the back membrane (Fig. 3.18d). The potential decreased from almost 6 V to 2 V over the cell when it is located in front of a pore. As shown

in the previous section, the potential starts decreasing earlier in front of the pore, due to the continuity between the channel and the pore, and this results in a larger electric field in front of the pores compared to polycarbonate parts of the porous membrane. Together with the collection of large amounts of charges at the close proximity of the pores, this early presence of large electric field seems to impose a significantly large potential drop over the back membrane when the cell is located in front of a pore.

This decrease of potential over very short distances (50 nm membrane thickness) resulted in extremely large electric field values over the cell structure. At this point, it should be kept in mind that the cell membrane thickness is 7-10 times larger than the real lipid bilayer thickness and more realistic electric field values can be obtained by multiplying the results by this correction factor. As shown in Fig. 3.20a, the largest electric field was found in the back membrane of the cell located in front of a pore, followed by the back membrane in front of the polycarbonate, the front membrane regardless of the location and finally the tight junction in front of the polycarbonate. The value of the electric field was approximately 6500 V/cm in the tight junction and it dropped to zero in the gap between the tight junction and the polycarbonate membrane (10 nm), corresponding to the constant potential inside the gap between the cell layer and the porous membrane (Fig. 3.20b). Inside the polycarbonate, the electric field jumped to larger values close to 7000 V/cm. This behavior was similar in the case of the cell located in front of the polycarbonate (Fig. 3.20c). The electric field dropped to almost zero in the gap between the cell structure and the polycarbonate; and then increased to 4000 V/cm inside the polycarbonate. However, in the latter scenario, the electric field in the back membrane of the cell structure reached much larger values, approximately 225,000 V/cm while the electric field in the front membrane was only around 70,000 V/cm.

In case of the cell structure located in front of a pore (Fig. 3.20d), there was no drop of electric field to zero inside the gap between the cell layer and the porous membrane. The electric field decreased gradually from extremely large values around 800,000 V/cm in the back membrane to its final value of 2000 V/cm inside the pore (Fig. 3.20d inset). The electric field inside the front membrane was similar to the case of the cell structure located in front of the polycarbonate. In both cases, the electric field remained almost zero inside the cytoplasm part of the cell structure.

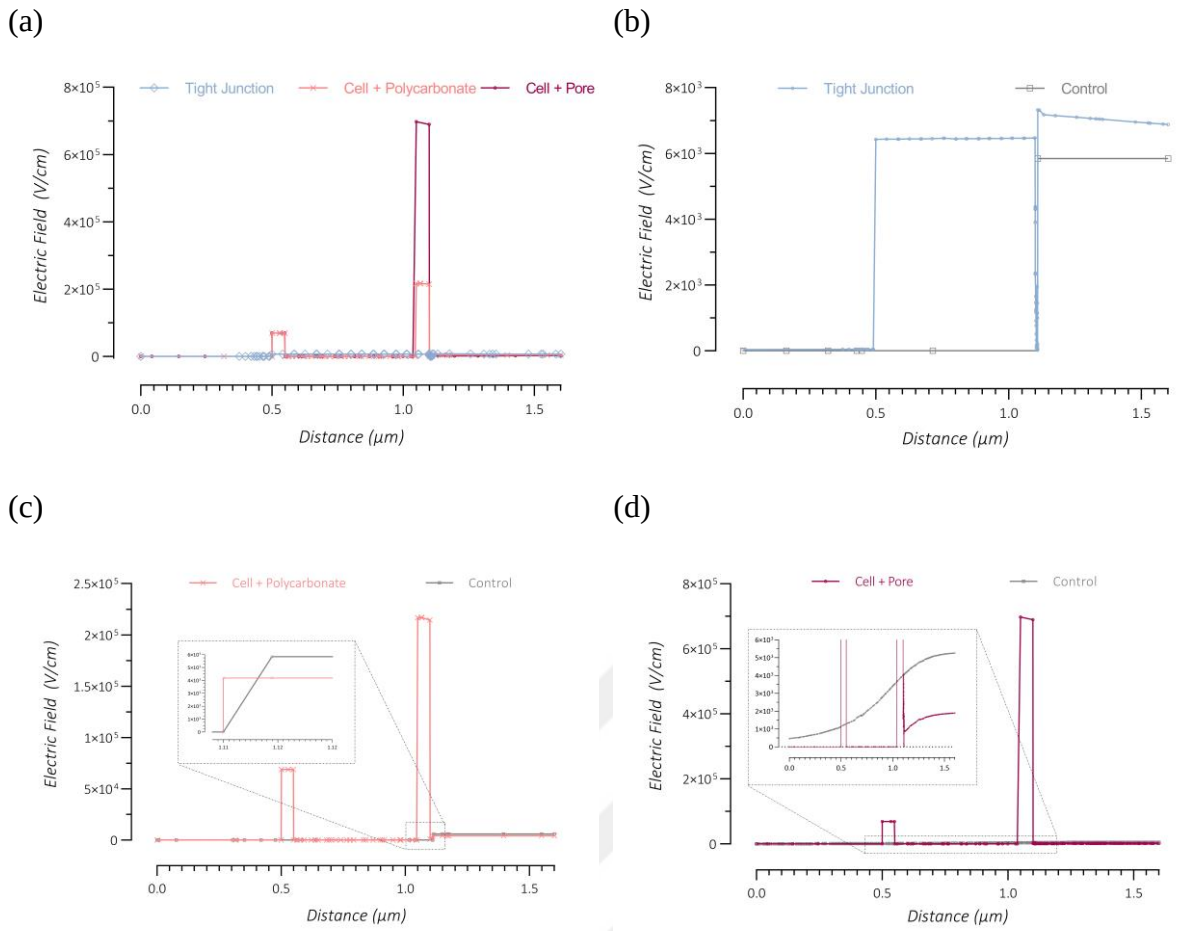

Figure 3.20. Electric field distribution over the cell layer in the multilayer configuration along the cutline passing either i) through a tight junction positioned in front of the polycarbonate, ii) through a cell positioned in front of the polycarbonate or iii) through a cell positioned in front of a pore

The electric field distribution results clearly show that there is a significant difference between the single-layer and the multi-layer configuration, even when a similar voltage-to-distance ratio is used. The major difference between the two systems was found on the back membrane of the cell layer; the electric field in the multilayer configuration in the back membrane was almost four times larger than the electric field induced in the back (and also the front) membrane of the cell layer in the single-layer configuration. This data suggests that there are several important points to be kept in mind when working with two systems simultaneously. First of all, the same applied voltage will have a significantly different result in the two chip configurations; the electric field on the cell layer in the multilayer configuration can easily acquire much larger values, which would increase the possibility of electroporation, and even cell disruption, while the electric field on the cell layer in the single-layer configuration can

easily be under the electroporation limit. This suggests that the thresholds for paracellular and transcellular permeabilization most probably will be completely different in the two systems.

Secondly, even when the applied potential is decreased in the multilayer configuration, this does not guarantee that a complete paracellular or a complete transcellular permeabilization via reversible electroporation will be achieved. Due to the extreme difference of electric field between the front and the back membrane in the cell layer, the effect of the electric field will be significantly different in two sides of the cell. For instance, it is quite possible that the front membrane and the cytoskeleton extending in this region will not be affected by electric field in low voltages, while the back membrane and the cytoskeleton extending in this region of the cell layer will still be disturbed even in very low voltages. This inhomogeneity may eventually lead to the disruption of cell homeostasis and following cellular apoptosis. Even if the electroporation can be achieved in a reversible manner, the pores will most probably localize in the back membrane of the cell layer and this will not have any use for the purpose of temporary permeabilization studies, where the aim is to transport specific molecules across the cell layer, not across only one side of the lipid bilayer.

Finally, an important point to consider is the effect of the electric field will depend on the location of the cell layer in the multilayer configuration. As seen in Fig. 3.20c and Fig. 3.20d, there is a significant difference in the electric field in the back membrane when it is located in front of a pore compared to when it is located in front of the polycarbonate region of the porous membrane. From this finding, it can be assumed that there will be major differences of the cell's response to the electric field depending on how close it is located to a pore. This may have two important consequences; the TEER measurements which do not provide spatial resolution may yield under/overestimation of the integrity of the cell layer and the localization of the transported species on particular regions, rather than a homogenous distribution behind the cell membrane. Same inhomogeneity can also be said for the paracellular permeabilization; depending on the location of the cell, not only the electric field on the cell membrane, but also the electric field on the tight junction changes, which may affect the current passing through the tight junctions and therefore, the distribution of the tight junction proteins.

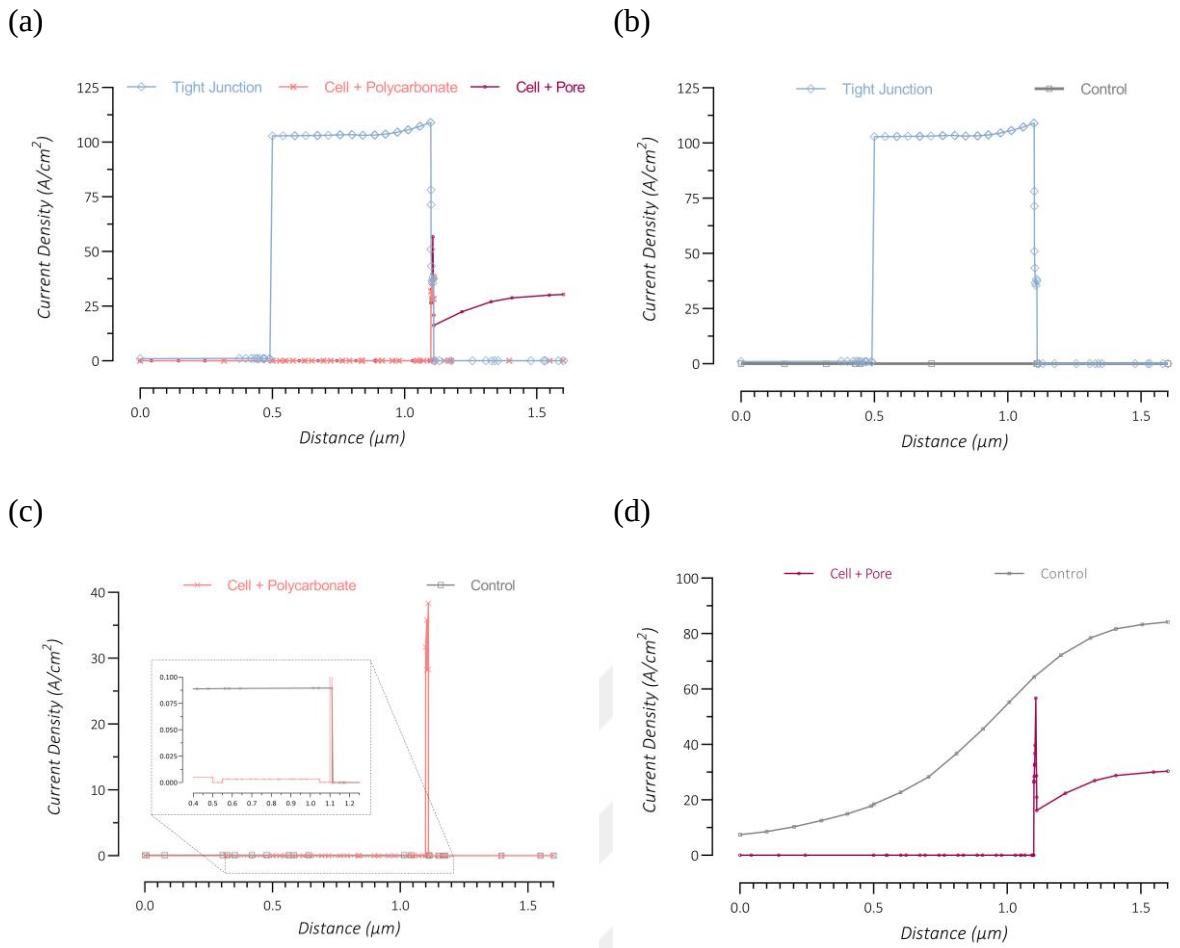

Figure 3.21. Current density distribution over the cell layer in the multilayer configuration along the cutline passing either i) through a tight junction positioned in front of the polycarbonate, ii) through a cell positioned in front of the polycarbonate or iii) through a cell positioned in front of a pore

As expected, the current density graphs (Fig. 3.21a and Fig. 3.21b) showed that the current in the system is not only localizing inside the pores as the previous case, but it is also localizing in the tight junctions before reaching to the porous membrane. The value of the current density is found to be 100 A/cm^2 for the tight junction while it was almost zero inside the cell structure regardless of the location. On the other hand, the value of the current density inside the cell layer was extremely low compared to tight junctions, which can be explained by the capacitance characteristics of the cell membrane and the large surface area of the cell layer. These results suggest that for a given conductivity of 10^{-7} and relative permittivity of 7, the current cannot pass though the cellular membrane at low frequencies and must pass through the tight junctions and then the pores inside the porous membrane. Even in this case, the current density was found to change significantly with respect to the location of the cells. Accordingly, the current density

in the back membrane of the cell located in front of a pore was approximately four times larger than that of the cell located in front of polycarbonate. Such difference was also observed between two sides of the cell layer; regardless of the location of the cell, the current density in the back membrane was one magnitude larger than the current density inside the front membrane. Overall, the current density results confirm the above considerations regarding the use of multilayer chip configuration for the pulsed electric field induced permeabilization studies.

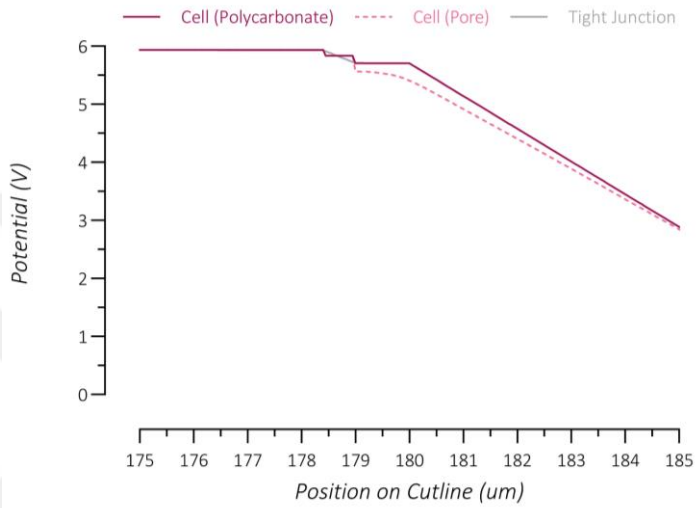

Figure 3.22. Effect of the distance of the cell layer from the polycarbonate membrane on the potential distribution over the cell layer

Lastly, these effects of the polycarbonate on the cell layer were shown to depend on the location of the cell layer. As shown in Fig. 3.22, once the cell layer is located 1-µm away from the polycarbonate, almost all differences with respect to the position of the cell membrane and the position of the cell itself diminished. Compared to the previous case where the cell layer was only 10 nm away from the polycarbonate, at larger distances the front and back membrane acquired an almost equal potential distribution regardless of the position of the cell layer with respect to the pores. This result confirms that the polycarbonate results in an accumulation of the charges surrounding the back membrane of the cell and this accumulation reaches to extreme levels in front of the pores, both effects can be reduced if the cell layer is kept relatively away from the polycarbonate membrane. In this respect, the single-layer chip configuration, where the cell layer is hanging by the stacks and it is perpendicular to the electrodes, holds an advantage. Even though cells are supported by the resistive PDMS pillars in two sides, these regions remain outside of the effective electric field region, unlike the gaps between PDMS pillars where the cell layer acts like suspended cells away from any insulator surface.

3.6 Effect of Frequency in the Single-Layer Configuration

Like studies conducted at fixed low frequency (1 Hz) that effectively acts like a direct current (DC), a small circuit equivalent can be used as an approximation in order to understand the behavior of structural elements for a given frequency range in alternated current (AC). As the frequency increases, the impedance of the structural elements gets dominated by the capacitive factor where the geometry and the dielectric constant play an important role. As most of the charges are collected at the two sides of the cell layer and, in case of a multilayer structure, the porous membrane, the capacitance of the BBB channel, brain chamber, tight junctions and the pores can be neglected.

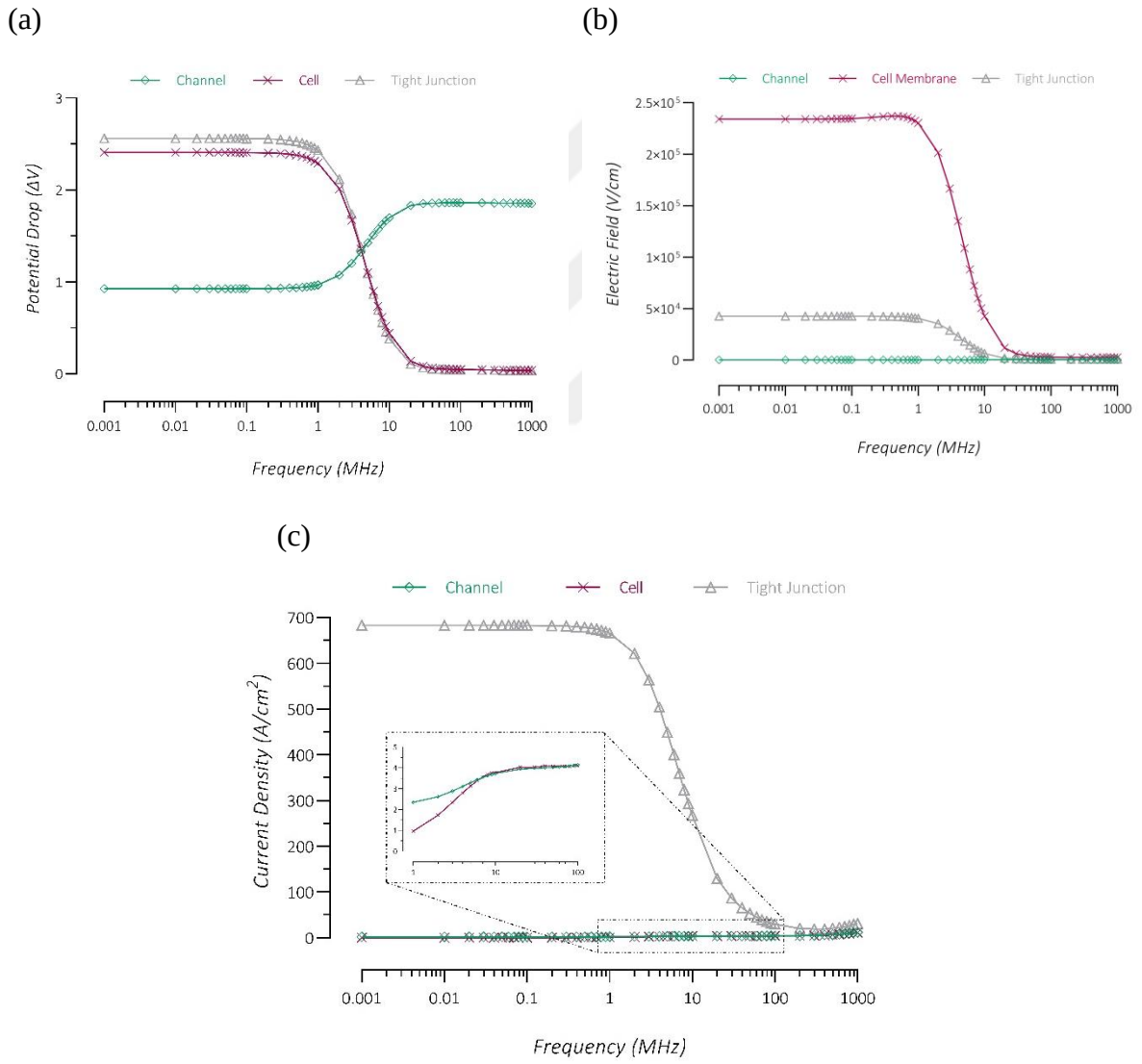

Figure 3.23. Frequency sweep analysis between 1 kHz and 1 GHz in the single layer configuration. a) potential drop, b) electric field and c) current density distribution over the selected structural elements

Frequency sweep analysis reveals frequency regions where the behavior of the cell layer significantly changes. In the single layer chip design, the total potential drop is distributed between two major elements, the channels and the cell layer. As can be seen in Fig. 3.23a, approximately between 1 and 20 MHz, the potential drop over the cell layer (and hence over the tight junctions) decreases, which corresponds to an increase of potential drop over the BBB channel and the brain chamber. This behavior can be explained by the decrease of capacitive impedance of the cell layer, which eventually becomes even lower than the resistance of the channel and the chamber. Even though in the literature the cell layer has shown to change its electrical behavior as early as 40 kHz, the potential distribution in the single-layer chip started to change significantly only after ~1 MHz. Like the potential distribution, the electric field value inside the cell membrane also significantly drops at early MHz regime and becomes constant eventually (Fig. 3.23b). However, it should be noted that even when the impedance of the cell layer is smaller than the channel resistance (smaller potential drop over the cell layer), the electric field remains approximately ten times larger than the electric field inside the rest of the structure and approximately three times larger than that of the tight junctions, which can be explained by the potential drop, however small it is, occurs over a very short distance (50 nm). On the other hand, the current density remains almost zero inside the cell layer in the kHz regime and only starts increasing significantly after ~1 MHz, accompanied by a proportional decrease of the current density inside the tight junctions for the conservation of the total current inside the system (Fig. 3.23c). Around ~10 MHz, the current density inside the cell layer becomes almost equal to that of the channels. This region draws attention for the purpose of the electric field induced permeability studies. Specifically for the single layer chip design, it seems that above 1 MHz, the possibility of transcellular permeabilization significantly increases until the cell becomes fully transparent to the current coming from the channels, on the other hand, paracellular permeabilization is expected to dominate at smaller frequencies. It should also be noted that regardless of the increase of the current density inside the cell layer, the current density value always remains larger inside the tight junctions due to its significantly smaller total surface area. This suggests that a direct relationship between the relative magnitude of the current density over the tight junctions and the cell layer and the possibility of paracellular and transcellular permeabilization cannot be constructed. For instance, even in the extreme low frequencies, where the current density is significantly larger than the cell layer, transcellular permeabilization and even irreversible electroporation have been shown to be possible. This requires the establishment of the current density threshold above which the electroporation starts in the cell membrane, regardless of how small it is compared to the tight junctions.

3.7 Effect of Frequency in the Multilayer Configuration

A similar analyses of different frequency regimes on the multilayer structure showed that the behavior of the cell layer is significantly different when located close to the porous membrane compared to the single chip design where the cell layer is surrounded by PBS in two sides. Unlike the single chip configuration, the total potential-drop over the cell layer showed a significant decrease in the kHz regime, namely after ~40 kHz, accompanied by a proportional increase of the potential drop over the porous membrane and no change of the potential drop over the channels (Fig. 3.24a). This result was in agreement with the literature, where the cell layer characteristics were shown to change above 40 kHz if the cells are located on top of an insulator support. This behavior can be explained by the fact that in the kHz regime, potential is mostly partitioned between two high impedance structural elements; the cell layer and the porous membrane. Having a larger capacitance than the porous membrane, the impedance of the cell layer decreases at smaller frequencies, which causes less potential to drop over the cell layer and leaves more of the potential to drop over the porous membrane. Only in the MHz regime, once the impedance of the porous membrane starts having similar values of channel resistance, the potential is distributed between the porous membrane and the channels, while there is no potential drop over the cell layer, and hence over the tight junctions (Fig. 3.24b). Even though the distribution is almost the same, it can be seen that the value of the potential drop over the cell located in front of polycarbonate is strictly different than that of the cell located in front of pore in all of the frequencies tested. As explained earlier, such difference disappears if the cell layer is located farther from the porous membrane.

As of the potential distribution, the electric field over the cell membrane decreased significantly after ~40 kHz, regardless of the location of the cell layer (Fig. 3.24c). However, the electric field in the cell layer located in front of a pore remained significantly larger until later frequencies around ~100 MHz while the electric field in the cell layer located in front of the polycarbonate was as small as that of the channels already at ~10 MHz. This suggests that the electric field response of the cell layer in the multilayer configuration will be inhomogeneous not only in the low frequency, but instead throughout the entire spectrum until the cell layer becomes electrically invisible around ~100 MHz, after which the cell layer cannot be used for temporary permeabilization purposes. As discussed earlier, this situation raises questions regarding the use of the multilayer chip configuration and shows that the main disadvantage of the system, i.e. the inhomogeneity of the electric field in the front and back membrane of the cell layer and in its location with respect to the pores, persists in all frequencies of interest.

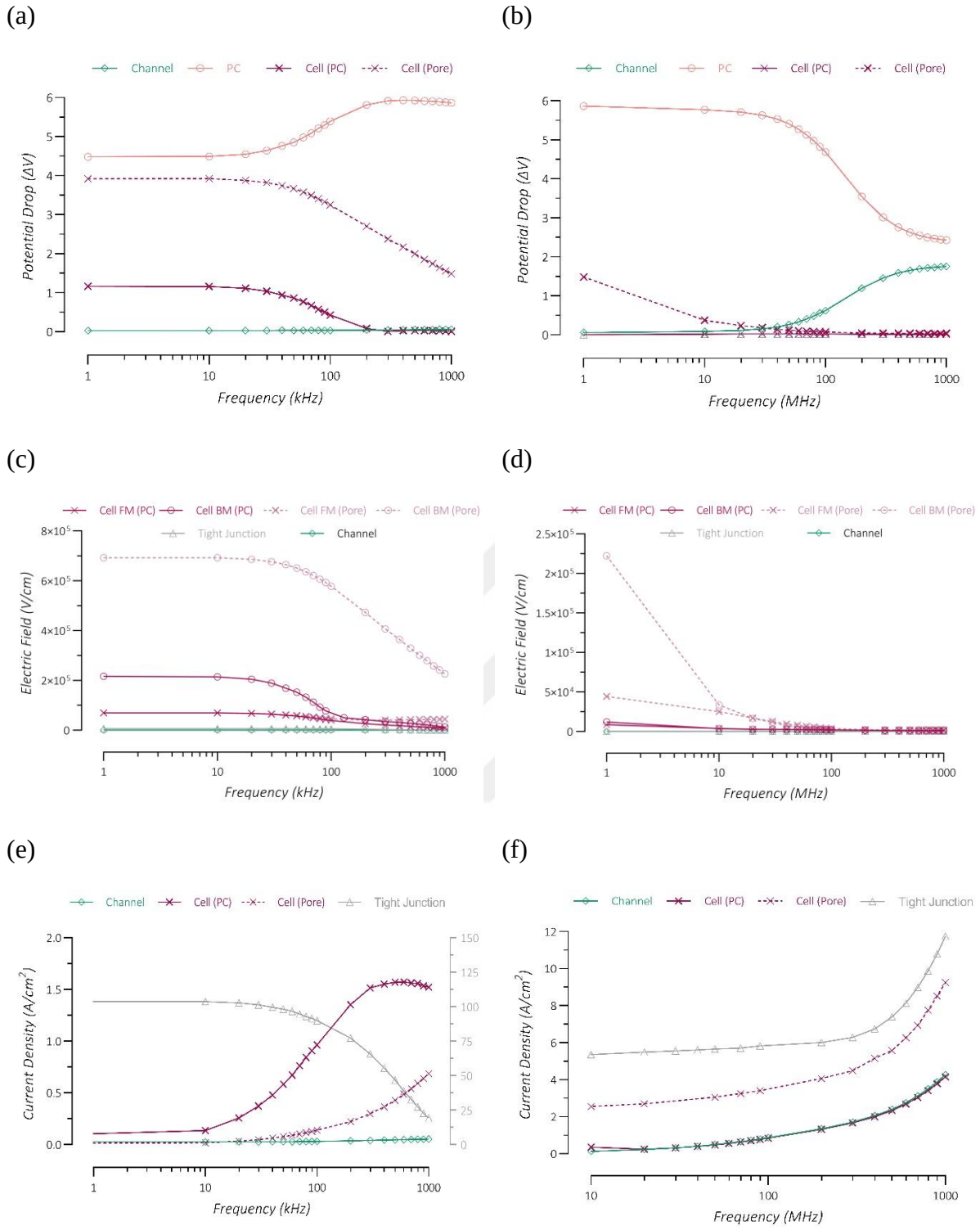

*Figure 3.24. Frequency sweep analysis between 1 kHz and 1 GHz in the multilayer configuration. a, b) potential; c, d) electric field and e, f) current density distribution over the selected structural elements. *The current density in the tight junction is plotted on the second y-axis in the kHz regime.*

Following this trend, the current density increases in the cell layer as the impedance decreases in the kHz regime, accompanied by a certain decrease of the current density in the tight junction (Fig. 3.24e). The behavior of the current density in these two main structural elements, was not completely complimentary, due to the difference between the current density in front of the polycarbonate and in front of pores. Starting from ~1 MHz, the current density inside the cell layer located in front of the polycarbonate acquires the same current density value of the channel (Fig. 3.24f). The current density inside the cell layer located in front of the pore follows the same distribution only with a slightly larger magnitude. All together, these results show that the current passing through the cell membrane increases significantly even in the low-kHz regime and the cell becomes transparent to current as early as ~1 MHz. This suggests that the frequency window for paracellular permeabilization is narrower in the multilayer structure compared to the single layer structure and the possibility of inducing electroporation increases significantly as soon as the applied frequency exceeds ~40 kHz.

4 CONCLUSION

In this study, two main configurations of BBB-on-a-chip were investigated for the possible use of applied electric field as an actuator for the permeability tuning of endothelial cell barrier. Simulation results showed that the induced electric field on the cell membrane can reach up to 250,000 V/cm in the single-layer chip configuration and up to 800,000 V/cm in the multi-layer chip configuration at low frequencies, compared to applied voltage-to-distance ratio of only 300 V/cm that is frequently used in the literature. On the other hand, the current density studies clearly showed that the current in the tight junctions were significantly larger than the current in the cell layer. This initial results illustrate the importance of supporting the experimental work by simulation-based theoretical studies where the small elements of the structures such as the cell membrane and the tight junctions can be addressed individually and be correlated with the results of the corresponding experiment for the better establishments of the differential effects of the electric field on the BBB permeabilization.

Comparison of the two chip configuration revealed that the single-layer chip configuration offers major advantages such as the homogenous distribution of the electric field in the cell layer and homogenous current density distribution in the tight junction, together with easier fabrication and individual permeability tuning of each cell layer between two PDMS pillars by the integrated small electrodes that focuses the electric field through the cell layer. Single-layer chip configuration was also optimized by testing different electrode configurations and the geometry was finalized such that both the electrodes placed consecutively and the electrodes with adequate distance between them can be used for electric field delivery simultaneously in the same experimental design, together with the control group where the endothelial cells will not be exposed to electric field. This property of the single-layer chip not only reduces the time and the effort spend on each experiment significantly, but also provides a more accurate and precise data throughout the structure. On the other hand, multilayer chip configuration revealed significant differences of electric field and current density distribution not only between two faces of the cell layer, but also between the position of the individual cells with respect to the pores in the polycarbonate membrane.

Actuator properties of the integrated electrodes were tested for a wide spectrum of frequencies up to 1 GHz. The results showed that the cell layer in the single-layer configuration behaves like suspended cells and becomes electrically invisible between 1 and 10 MHz. This suggests that the electric field for the permeabilization can only be used until approximately 10 MHz, above which the cell layer is expected to disintegrate irreversibly. On the other hand, the cell

layer that is attached on the polycarbonate membrane was shown to become electrically invisible at much earlier frequencies around 40 kHz. The frequency range where the cell layer still acquires a certain impedance to oppose the current, however, lasted all the way up to 100 MHz. This was the direct consequence of major difference between the cells located in front of polycarbonate and the cells located in front of the pores. Even though the response of the cell layer against the applied electric field changes over a much larger frequency range in the multilayer chip configuration, the inhomogeneities of the electric field and current density distribution persist throughout this entire region, which makes any possible permeability tuning in the multilayer configuration less accurate and significantly less precise. These findings, together with the problems during the fabrication, i.e. alignment of the different channels and electrodes layers, and the problems with the direct visualization under the microscope, the multilayer chip configuration suffers from major drawbacks with respect to its use for the PEF-induced permeabilization studies.

It is also important to consider the drawbacks in this simulation-based study. As explained earlier, the 3D model lacked some of the realistic conditions. For instance, the thickness of the cell membrane was increased to 50 nm from its more physiologically relevant values of 5-10 nm. This was a compromise made to be able to introduce more relatively large number of cells, which has not been done in the literature to best of our knowledge. Similarly, the tight junctions between the endothelial cells were depicted as 10 nm. Even though it is shown in the literature that the tight junctions can change significantly with the introduction of important contributors, for instance other CNS cells and the shear stress, the fully developed tight junctions might be as small as 2 nm. However, most of the BBB-on-a-chip construct fails to regenerate the *in vivo* BBB conditions with the fully developed tight junctions. For this reason, it is very important to measure the thickness of the tight junctions during the BBB-on-a-chip applications and correlate it with the TEER measurements. This way, the numbers presented in this study for the 10 nm tight junction thickness can easily be converted to experimental condition by applying a simple correction factor for the size. Similarly, the electric field and the current density values obtained for the cell membrane can also be converted to their more realistic equivalents by the introduction of a size correction factor. For instance, if the average thickness of the endothelial cell line used in the experiment is five time smaller, the electric field values obtained in this study can be multiplied by five to obtain an approximated value for the electric field induced in 10 nm endothelial membrane.

5 FUTURE PERSPECTIVES

It is important to consider that the model presented in this study requires an experimental confirmation in the future. Accordingly, the two chip configurations will be fabricated as designed in the first section of this thesis and the initial optimizations for fully functioning BBB in the present of astrocytes, pericytes and the shear stress will be carried out. The integrity of the cell layer will be measured before and after the endothelial cells are seeded using integrated electrodes as sensors of TEER impedance spectroscopy. The change of permeability will be tracked for not only different magnitudes and frequencies of the electric fields applied, but also for different pulse numbers and pulse durations. Lastly, the experimental results will be correlated with the corresponding simulation-based study to establish the thresholds for the paracellular and transcellular permeabilization while keeping the cell viability in consideration to stay under the irreversible electroporation limit.

REFERENCES

Abbott, N. J., Patabendige, A. A., Dolman, D. E., Yusof, S. R., & Begley, D. J. (2010). Structure and function of the blood–brain barrier. *Neurobiology of disease*, *37*(1), 13-25.

Abbott, N. J., Rönnbäck, L., & Hansson, E. (2006). Astrocyte–endothelial interactions at the blood–brain barrier. *Nature reviews neuroscience*, *7*(1), 41.

Achyuta, A.K.H., Conway, A.J., Crouse, R.B., Bannister, E.C., Lee, R.N., Katnik, C.P., Behensky, A.A., Cuevas, J. and Sundaram, S.S., (2013). A modular approach to create a neurovascular unit-on-a-chip. *Lab on a Chip*, *13*(4), 542-553.

Agerholm-Larsen, B., Iversen, H. K., Ibsen, P., Moller, J. M., Mahmood, F., Jensen, K. S., & Gehl, J. (2011). Preclinical validation of electrochemotherapy as an effective treatment for brain tumors. *Cancer research*, *71*(11), 3753-3762.

Andreone, B. J., Lacoste, B., & Gu, C. (2015). Neuronal and vascular interactions. *Annual review of neuroscience*, *38*, 25-46.

Arena, C. B., Garcia, P. A., Sano, M. B., Olson, J. D., Rogers-Cotrone, T., Rossmeisl Jr, J. H., & Davalos, R. V. (2014). Focal blood-brain-barrier disruption with high-frequency pulsed electric fields. *Technology*, *2*(03), 206-213.

Bard, A. J., & Faulkner, L. R. (2001). Fundamentals and applications. *Electrochemical Methods*, *2*(482), 580-632.

Blinder, P., Tsai, P. S., Kaufhold, J. P., Knutsen, P. M., Suhl, H., & Kleinfeld, D. (2013). The cortical angiome: an interconnected vascular network with noncolumnar patterns of blood flow. *Nature neuroscience*, *16*(7), 889.

Bonakdar, M., Graybill, P. M., & Davalos, R. V. (2017). A microfluidic model of the blood–brain barrier to study permeabilization by pulsed electric fields. *RSC advances*, *7*(68), 42811-42818.

Bonakdar, M., Wasson, E. M., Lee, Y. W., & Davalos, R. V. (2016). Electroporation of brain endothelial cells on chip toward permeabilizing the blood-brain barrier. *Biophysical journal*, *110*(2), 503-513.

Booth, R., & Kim, H. (2012). Characterization of a microfluidic in vitro model of the blood-brain barrier (μBBB). *Lab on a Chip*, *12*(10), 1784-1792.

Brightman, M. W., & Kadota, Y. (1993). Nonpermeable and permeable vessels of the brain. *NIDA research monograph*, *120*, 87-87.

Brown, J.A., Pensabene, V., Markov, D.A., Allwardt, V., Neely, M.D., Shi, M., Britt, C.M., Hoilett, O.S., Yang, Q., Brewer, B.M. and Samson, P.C., (2015). Recreating blood-brain barrier physiology and structure on chip: A novel neurovascular microfluidic bioreactor. *Biomicrofluidics*, *9*(5), 054124.

Davalos, R. V., Mir, L. M., & Rubinsky, B. (2005). Tissue ablation with irreversible electroporation. *Annals of biomedical engineering*, *33*(2), 223.

Deosarkar, S. P., Prabhakarpandian, B., Wang, B., Sheffield, J. B., Krynska, B., & Kiani, M. F. (2015). A novel dynamic neonatal blood-brain barrier on a chip. *PloS One*, *10*(11), e0142725.

Elbrecht, D. H., Long, C. J., & Hickman, J. J. (2016). Transepithelial/endothelial Electrical Resistance (TEER) theory and ap-plications for microfluidic body-on-a-chip devices. *tc*, *1*(1), 1.

Farkas, E., & Luiten, P. G. (2001). Cerebral microvascular pathology in aging and Alzheimer's disease. *Progress in neurobiology*, *64*(6), 575-611.

Garcia, P. A., Rossmeisl Jr, J. H., Robertson, J. L., Olson, J. D., Johnson, A. J., Ellis, T. L., & Davalos, R. V. (2012). 7.0-T magnetic resonance imaging characterization of acute blood-brain-barrier disruption achieved with intracranial irreversible electroporation. *PloS one*, *7*(11), e50482.

Griep, L.M., Wolbers, F., de Wagenaar, B., ter Braak, P.M., Weksler, B.B., Romero, I.A., Couraud, P.O., Vermes, I., van der Meer, A.D. and van den Berg, A., (2013). BBB on chip: microfluidic platform to mechanically and biochemically modulate blood-brain barrier function. *Biomedical microdevices*, *15*(1), 145-150.

Henry, O. Y., Villenave, R., Cronce, M. J., Leineweber, W. D., Benz, M. A., & Ingber, D. E. (2017). Organs-on-chips with integrated electrodes for trans-epithelial electrical resistance (TEER) measurements of human epithelial barrier function. *Lab on a Chip*, *17*(13), 2264-2271.

Herland, A., van der Meer, A. D., FitzGerald, E. A., Park, T. E., Sleeboom, J. J., & Ingber, D. E. (2016). Distinct contributions of astrocytes and pericytes to neuroinflammation identified in a 3D human blood-brain barrier on a chip. *PLoS One, 11*(3), e0150360.

Hjouj, M., Last, D., Guez, D., Daniels, D., Sharabi, S., Lavee, J., Rubinsky, B. and Mardor, Y., (2012). MRI study on reversible and irreversible electroporation induced blood brain barrier disruption. *PloS One, 7*(8), p.e42817.

Hori, S., Ohtsuki, S., Hosoya, K. I., Nakashima, E., & Terasaki, T. (2004). A pericyte-derived angiopoietin-1 multimeric complex induces occludin gene expression in brain capillary endothelial cells through Tie-2 activation in vitro. *Journal of neurochemistry, 89*(2), 503-513.

Hynynen, K., McDannold, N., Sheikov, N. A., Jolesz, F. A., & Vykhodtseva, N. (2005). Local and reversible blood–brain barrier disruption by noninvasive focused ultrasound at frequencies suitable for trans-skull sonications. *Neuroimage*, *24*(1), 12-20.

Jayasooriya, V., & Nawarathna, D. (2017). Simulation of molecular transport through an electroporated cell using COMSOL Multiphysics. In 13th COMSOL conference, Boston.

Jou, T. S., Schneeberger, E. E., & James Nelson, W. (1998). Structural and functional regulation of tight junctions by RhoA and Rac1 small GTPases. *The Journal of cell biology, 142*(1), 101-115.

Kotnik, T., Pucihar, G., & Miklavčič, D. (2010). Induced transmembrane voltage and its correlation with electroporation-mediated molecular transport. *The Journal of membrane biology, 236*(1), 3-13.

Kroll, R. A., Neuwelt, E. A., & Neuwelt, E. A. (1998). Outwitting the blood-brain barrier for therapeutic purposes: osmotic opening and other means. *Neurosurgery, 42*(5), 1083-1099.

Lee, S.W., Kim, W.J., Choi, Y.K., Song, H.S., Son, M.J., Gelman, I.H., Kim, Y.J. and Kim, K.W., (2003). SSeCKS regulates angiogenesis and tight junction formation in blood-brain barrier. *Nature medicine, 9*(7), 900-906.

Levanony, H., Rubin, R., Altschuler, Y., & Galili, G. (1992). Evidence for a novel route of wheat storage proteins to vacuoles. *The Journal of Cell Biology, 119*(5), 1117-1128.

Li, S., Chen, X., & Han, F. (2018). Simulation of Cell Dielectric Properties Based on COMSOL. *Journal of Robotics, Networking and Artificial Life, 4*(4), 330-333.

Liebner, S., Fischmann, A., Rascher, G., Duffner, F., Grote, E. H., Kalbacher, H., & Wolburg, H. (2000). Claudin-1 and claudin-5 expression and tight junction morphology are altered in blood vessels of human glioblastoma multiforme. *Acta neuropathologica, 100*(3), 323-331.

Lindahl, P., Johansson, B. R., Levéen, P., & Betsholtz, C. (1997). Pericyte loss and microaneurysm formation in PDGF-B-deficient mice. *Science, 277*(5323), 242-245.

Linville, R.M., DeStefano, J.G., Sklar, M.B., Xu, Z., Farrell, A.M., Bogorad, M.I., Chu, C., Walczak, P., Cheng, L., Mahairaki, V. and Whartenby, K.A., (2019). Human iPSC-derived blood-brain barrier microvessels: Validation of barrier function and endothelial cell behavior. *Biomaterials, 190*, 24-37.

Liu, H.L., Hua, M.Y., Chen, P.Y., Chu, P.C., Pan, C.H., Yang, H.W., Huang, C.Y., Wang, J.J., Yen, T.C. and Wei, K.C., (2010). Blood-brain barrier disruption with focused ultrasound enhances delivery of chemotherapeutic drugs for glioblastoma treatment. *Radiology, 255*(2), 415-425.

Lopez-Quintero, S. V., Datta, A., Amaya, R., Elwassif, M., Bikson, M., & Tarbell, J. M. (2010). DBS-relevant electric fields increase hydraulic conductivity of in vitro endothelial monolayers. *Journal of neural engineering, 7*(1), 016005.

M Fu, B. (2012). Experimental methods and transport models for drug delivery across the blood-brain barrier. *Current pharmaceutical biotechnology, 13*(7), 1346-1359.

Marino, A., Tricinci, O., Battaglini, M., Filippeschi, C., Mattoli, V., Sinibaldi, E., & Ciofani, G. (2018). A 3D Real-Scale, Biomimetic, and Biohybrid Model of the Blood-Brain Barrier Fabricated through Two-Photon Lithography. *Small, 14*(6), 1702959.

Meulenberg, C. J., Todorovic, V., & Cemazar, M. (2012). Differential cellular effects of electroporation and electrochemotherapy in monolayers of human microvascular endothelial cells. *PLoS One, 7*(12), e52713.

Mir, M., Lagunas, A., Palma., S., Lopez, M.J., Samitier, J. (2020) Brain Blood Barrier sensing in organ-on-a-chip; beyond TEER. Manuscript submitted for publication.

Murovec, T., Sweeney, D. C., Latouche, E., Davalos, R. V., & Brosseau, C. (2016). Modeling of transmembrane potential in realistic multicellular structures before electroporation. *Biophysical journal*, *111*(10), 2286-2295.

Nicaise, C., Mitrecic, D., Demetter, P., De Decker, R., Authelet, M., Boom, A., & Pochet, R. (2009). Impaired blood–brain and blood–spinal cord barriers in mutant SOD1-linked ALS rat. *Brain research*, *1301*, 152-162.

Niego, B. E., & Medcalf, R. L. (2013). Improved method for the preparation of a human cell-based, contact model of the blood-brain barrier. *JoVE (Journal of Visualized Experiments)*, (81), e50934.

Oller-Salvia, B., Sánchez-Navarro, M., Giralt, E., & Teixidó, M. (2016). Blood–brain barrier shuttle peptides: an emerging paradigm for brain delivery. *Chemical Society Reviews*, *45*(17), 4690-4707.

Partyka, P. P., Godsey, G. A., Galie, J. R., Kosciuk, M. C., Acharya, N. K., Nagele, R. G., & Galie, P. A. (2017). Mechanical stress regulates transport in a compliant 3D model of the blood-brain barrier. *Biomaterials*, *115*, 30-39.

Peppiatt, C. M., Howarth, C., Mobbs, P., & Attwell, D. (2006). Bidirectional control of CNS capillary diameter by pericytes. *Nature*, *443*(7112), 700-704.

Perlmutter, L. S., & Chui, H. C. (1990). Microangiopathy, the vascular basement membrane and Alzheimer's disease: a review. *Brain research bulletin*, *24*(5), 677-686.

Petty, M. A., & Lo, E. H. (2002). Junctional complexes of the blood–brain barrier: permeability changes in neuroinflammation. Progress in neurobiology, 68(5), 311-323.

Prabhakarpandian, B., Shen, M. C., Nichols, J. B., Mills, I. R., Sidoryk-Wegrzynowicz, M., Aschner, M., & Pant, K. (2013). SyM-BBB: a microfluidic blood brain barrier model. *Lab on a Chip*, *13*(6), 1093-1101.

Rubin, L. L. (1992). Endothelial cells: adhesion and tight junctions. *Current opinion in cell biology*, *4*(5), 830-833.

Sano, M. B., Arena, C. B., DeWitt, M. R., Saur, D., & Davalos, R. V. (2014). In-vitro bipolar nano-and microsecond electro-pulse bursts for irreversible electroporation therapies. *Bioelectrochemistry*, *100*, 69-79.

Santaguida, S., Janigro, D., Hossain, M., Oby, E., Rapp, E., & Cucullo, L. (2006). Side by side comparison between dynamic versus static models of blood–brain barrier in vitro: a permeability study. *Brain research, 1109*(1), 1-13.

Schreibelt, G., Kooij, G., Reijerkerk, A., van Doorn, R., Gringhuis, S.I., van der Pol, S., Weksler, B.B., Romero, I.A., Couraud, P.O., Piontek, J. and Blasig, I.E., (2007). Reactive oxygen species alter brain endothelial tight junction dynamics via RhoA, PI3 kinase, and PKB signaling. *The FASEB Journal*, *21*(13), 3666-3676.

Sharabi, S., Bresler, Y., Ravid, O., Shemesh, C., Atrakchi, D., Schnaider-Beeri, M., Gosselet, F., Dehouck, L., Last, D., Guez, D. and Daniels, D., (2019). Transient blood–brain barrier disruption is induced by low pulsed electrical fields in vitro: an analysis of permeability and trans-endothelial electric resistivity. *Drug delivery*, *26*(1), 459-469.

Srinivasan, B., Kolli, A. R., Esch, M. B., Abaci, H. E., Shuler, M. L., & Hickman, J. J. (2015). TEER measurement techniques for in vitro barrier model systems. *Journal of laboratory automation, 20*(2), 107-126.

Taghian, T., Narmoneva, D. A., & Kogan, A. B. (2015). Modulation of cell function by electric field: a high-resolution analysis. *Journal of the Royal Society Interface, 12*(107), 20150153.

Treat, L. H., McDannold, N., Vykhodtseva, N., Zhang, Y., Tam, K., & Hynynen, K. (2007). Targeted delivery of doxorubicin to the rat brain at therapeutic levels using MRI-guided focused ultrasound. *International journal of cancer, 121*(4), 901-907.

van Der Helm, M. W., Van Der Meer, A. D., Eijkel, J. C., van den Berg, A., & Segerink, L. I. (2016). Microfluidic organ-on-chip technology for blood-brain barrier research. *Tissue barriers, 4*(1), e1142493.

Vitek, J. L. (2008). Deep brain stimulation: how does it work? *Cleveland Clinic journal of medicine, 75*(2), S59.

Walter, F.R., Valkai, S., Kincses, A., Petneházi, A., Czeller, T., Veszelka, S., Ormos, P., Deli, M.A. and Dér, A., (2016). A versatile lab-on-a-chip tool for modeling biological barriers. Sensors and Actuators B: *Chemical, 222*,1209-1219.

Wang, J. D., Khafagy, E. S., Khanafer, K., Takayama, S., & ElSayed, M. E. (2016). Organization of endothelial cells, pericytes, and astrocytes into a 3D microfluidic in vitro model of the blood–brain Barrier. *Molecular pharmaceutics, 13*(3), 895-906.

Warren, K., Jakacki, R., Widemann, B., Aikin, A., Libucha, M., Packer, R., Vezina, G., Reaman, G., Shaw, D., Krailo, M. and Osborne, C., (2006). Phase II trial of intravenous lobradimil and carboplatin in childhood brain tumors: a report from the Children's Oncology Group. *Cancer chemotherapy and pharmacology, 58*(3), 343.

Winkler, E. A., Bell, R. D., & Zlokovic, B. V. (2011). Central nervous system pericytes in health and disease. *Nature neuroscience, 14*(11), 1398.

Wolburg, H., & Lippoldt, A. (2002). Tight junctions of the blood–brain barrier: development, composition and regulation. *Vascular pharmacology, 38*(6), 323-337.

Wolburg, H., Wolburg-Buchholz, K., Liebner, S., & Engelhardt, B. (2001). Claudin-1, claudin-2 and claudin-11 are present in tight junctions of choroid plexus epithelium of the mouse. *Neuroscience letters, 307*(2), 77-80.

Wolff, A., Antfolk, M., Brodin, B., & Tenje, M. (2015). In vitro blood–brain barrier models—an overview of established models and new microfluidic approaches. *Journal of pharmaceutical sciences, 104*(9), 2727-2746.

Wosik, K., Cayrol, R., Dodelet-Devillers, A., Berthelet, F., Bernard, M., Moumdjian, R., Bouthillier, A., Reudelhuber, T.L. and Prat, A., (2007). Angiotensin II controls occludin function and is required for blood–brain barrier maintenance: relevance to multiple sclerosis. *Journal of Neuroscience, 27*(34), 9032-9042.

Xu, H., Li, Z., Yu, Y., Sizdahkhani, S., Ho, W.S., Yin, F., Wang, L., Zhu, G., Zhang, M., Jiang, L. and Zhuang, Z., (2016). A dynamic in vivo-like organotypic blood-brain barrier model to probe metastatic brain tumors. *Scientific reports, 6*, p.36670.

Yamamoto, M., Ramirez, S.H., Sato, S., Kiyota, T., Cerny, R.L., Kaibuchi, K., Persidsky, Y. and Ikezu, T., (2008). Phosphorylation of claudin-5 and occludin by rho kinase in brain endothelial cells. *The American journal of pathology, 172*(2), 521-533.

Yong, V. W. (2005). Metalloproteinases: mediators of pathology and regeneration in the CNS. *Nature Reviews Neuroscience, 6*(12), 931-944.

Zhou, J. X., Ding, G. R., Zhang, J., Zhou, Y. C., Zhang, Y. J., & Guo, G. Z. (2013). Detrimental effect of electromagnetic pulse exposure on permeability of in vitro blood-brain-barrier model. *Biomedical and Environmental Sciences, 26*(2), 128-137.

Zlokovic, B. V. (2011). Neurovascular pathways to neurodegeneration in Alzheimer's disease and other disorders. *Nature Reviews Neuroscience, 12*(12), 723-738.